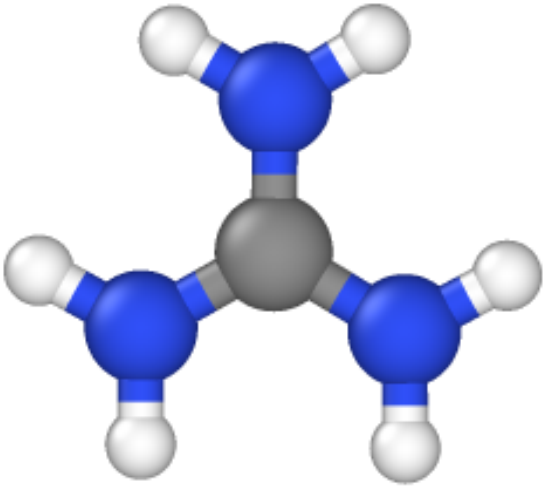

Modeling the effect of guanidinium in hybrid halide perovskites

Development of a neuro evolution potential for hybrid halide perovskite containing guanidinium

Master's thesis in Physics

Rickard Dahlgren Blumenau

DEPARTMENT OF CONDENSED MATTER PHYSICS

CHALMERS UNIVERSITY OF TECHNOLOGY
Gothenburg, Sweden 2025
www.chalmers.se

Master's thesis 2025

Modeling the effect of guanidinium in hybrid halide perovskites

Development of a neuro evolution potential for hybrid halide perovskite containing guanidinium

Rickard Dahlgren Blumenau

CHALMERS
UNIVERSITY OF TECHNOLOGY

Department of Physics
Division of Condensed Matter Physics
Wiktor Group
Chalmers University of Technology
Gothenburg, Sweden 2025

Modeling the effect of guanidinium in hybrid halide perovskites
Development of a neuro evolution potential for hybrid halide perovskite containing guanidinium
Rickard Dahlgren Blumenau

Supervisor: Sangita Dutta, Department of Physics
Examiner: Julia Wiktor, Department of Physics

Master's Thesis 2025
Department of Physics
Division of Condensed Matter Physics
Wiktor Group
Chalmers University of Technology
SE-412 96 Gothenburg
Telephone +46 31 772 1000

Cover: Guanidinium molecule

Typeset in LaTeX
Printed by Chalmers Reproservice
Gothenburg, Sweden 2025

Modeling the effect of guanidinium in hybrid halide perovskites
Development of a neuro evolution potential for hybrid halide perovskite containing guanidinium
Rickard Dahlgren Blumenau
Department of Physics
Chalmers University of Technology

Abstract

Hybrid halide perovskites have in recent years been one of the most rapidly advancing solar cell technologies. However, they face many issues especially related to stability, since in general they easily degrade into photo-inactive phases due to environmental factors like temperature, humidity and light. It is thus of interest to understand the phase behaviors of these systems to be able to engineer stable perovskite solar cells with favorable optoelectronic properties. Two of the most promising organic halide perovskites for solar cells are $MAPbI_3$ (MAPI) and $FAPbI_3$ (FAPI). By mixing these it is possible to tune the optoelectronic properties and phase behavior. In recent studies it has been shown that incorporating $GUAPbI_3$ (GUAPI) could further improve the optoelectronic properties by for instance increasing the charge carrier lifetime. However, the exact phase behaviors of these systems have not been investigated extensively. Thus, in this thesis the temperature dependence of the phase behaviors of mixed (MA,FA,GUA)PbI_3 as well as each pure systems were investigated by training a neuro evolution potential (NEP) model on structural properties calculated through density functional theory (DFT). The model predicted the previously known phase behaviors of FAPI and MAPI. Additionally, the morphotropic phase boundary (MPB) between MAPI and FAPI was found around 21% of FAPI, which is in agreement with previous studies. GUAPI was found to adopt the $a^-a^-a^-$ phase at temperatures below 280 K. Furthermore, it was found that adding GUAPI to (MA,FA)PbI_3 the MPB shifted towards higher FAPI concentrations.

Keywords: neuro evolution potential, density functional theory, molecular dynamics, perovskites, guanidinium

Acknowledgements

I would like to thank my examiner Julia Wiktor for giving me the opportunity to do this master thesis. It has been a very interesting topic. Additionally, I would like to thank Sangita Dutta and Erik Fransson for good supervision. You have provided many interesting ideas and discussions throughout the project. Your guidance have been very appreciated.

Rickard Dahlgren Blumenau, Gothenburg, August 2025

List of Acronyms

Below is the list of acronyms that have been used throughout this thesis listed in alphabetical order:

DFT	Density Functional Theory
MACE	Machine-learned Atomic Cluster Expansion
MD	Molecular dynamics
MPB	Morphotropic Phase Boundary
NEP	Neuro evolution potential
NpT	Isothermal-isobaric ensemble
NVE	Microcanonical ensemble
PES	Potential energy surface
VASP	Vienna Ab initio Simulation Package

Contents

List of Figures

1
Introduction

1.1 Background

In recent years, perovskites have emerged as promising materials for solar cells. This is because of their low-cost potential, defect tolerance and high efficiency [1, 2]. Currently, it has been possible to achieve power conversion efficiencies of over 25%, rivaling many state-of-the-art technologies [3]. However, perovskite solar cells tend to suffer from stability issues. Their phase is usually sensitive to environmental conditions like temperature, moisture and light. This is an issue since not every phase is photoactive and thus suitable for photovoltaic applications [1].
The perovskites for which the highest efficiencies have been achieved are so called hybrid halide perovskites. Two of the most promising hybrid halide perovskites are $MAPbI_3$ (MAPI) and $FAPbI_3$ (FAPI). This is in large part due to their bandgap of 1.55 eV and 1.47 eV, respectively [1], which is close to the optimal one to absorb photons from the solar spectrum according to the Shockley-Queisser limit [4]. FA ($CH[NH_2]_2$) is slightly larger than MA (CH_3NH_3), which results in different distortions of the lattice and thus differences in their phase diagrams and optoelectronic properties. The difference is not only related to the size difference, but also properties like vibration modes and dipole moments [5]. By mixing the two materials, it is possible to tune the properties to achieve higher stability and efficiency [1, 6]. However, there are still stability issues and a possible solution could be to use an even larger organic molecule, GUA ($C[NH_2]_3$). It has for instance been shown experimentally that this can increase the charge carrier life-time and stability [5]. However, most thermodynamic properties, like the phase behavior in triple cation (MA,FA,GUA)PbI_3 are still relatively unexplored. The dynamics can be quite accurately explored using density functional theory (DFT), however this is usually computationally heavy. It is thus of interest to create a machine learning model that can accurately predict the phase transitions and dynamics of the material without the same computational cost as DFT.

1.2 Aim

The aim of this thesis is to train a neuro evolution potential (NEP) model using Graphics Processing Unit Molecular Dynamics (GPUMD) [7] software based on a training dataset obtained from DFT calculations. This will first be done for pure $GUAPbI_3$ and the model will then be extended to the mixed systems, $GUA_{1-x-y}MA_xFA_yPbI_3$ for $x \in [0, 1]$, $y \in [0, 1-x]$. To efficiently generate a rich

initial set of structures, machine-learned atomic cluster expansion (MACE) [8] potentials will be utilized. The trained NEP models for pure and mixed systems will be used to perform molecular dynamics (MD) simulations on larger pure and mixed crystals respectively to understand the phase transitions and related properties.

1.3 Limitations

Phase transitions can occur due to many different environmental factors, but this thesis will be limited to phase transitions caused by temperature changes and not other environmental factors like pressure, moisture or light.
Furthermore, larger systems than 50 000 atoms will not be explored because of the associated computational cost of investigating even larger systems. Based on earlier studies of different hybrid halide perovskites, this size should be enough to find the general phase behaviors, however possible patterns emerging as two phases coexist might not be detected. For instance the twinning pattern of mixed (MA,FA)PbI_3 will probably not be detectable, since it required over one million atoms to detect in a similar study [9].
These systems will be simulated using periodic boundary conditions, since the study is limited to the bulk properties of the perovskites. Thus, surface effects are not in the scope of this thesis.
Since DFT is more computationally heavy than machine-learned potentials, the system size of the training and test data will be limited to a few 100s of atoms. When using MD with the final NEP model it will be possible to generalize to larger structures while at the same time reducing the computational time significantly, which will be helpful to eliminate finite-size effects.

2

Theory and Methology

2.1 Hybrid halide perovskites

Perovskites are a class of materials with a crystal structure that is defined by the chemical formula ABX_3 ordered in a repeating grid of BX_6 octahedras with the A-site occupying the vacancy formed by these grids as can be seen in Figure 2.1 [10]. The A-site is occupied by a monovalent cation, the B-site is occupied by a divalent cation and the X-site is occupied by an anion. Hybrid halide perovskites are the subset of perovskites for which the monovalent cation is an organic molecule and the anion is a halide.

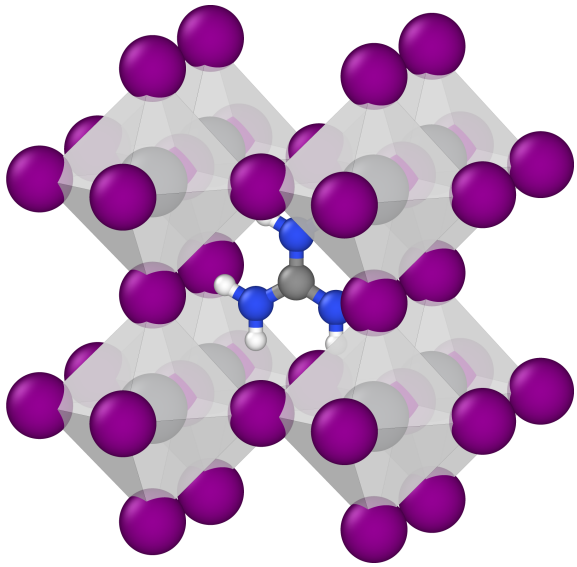

Figure 2.1: Perovskite structure (ABX_3). The purple atoms are the X-sites, the grey atoms inside the transparent octahedra are the B-sites and the molecule in the center is the A-site.

There are many different varieties of perovskites, but the ones that are of interest in this thesis are 3D corner-sharing perovskites, since they generally are the most photoactive forms [11]. 3D corner-sharing perovskites are characterized by the structure seen in Figure 2.1 being continually repeated in all three dimensions. The name originates from each octahedron sharing corners with the neighboring octahedra in every cartesian direction.
3D corner-sharing perovskites can exist in different phases caused by the tilt of the octahedra. The tilt of the octahedra is related to the M- and R-phonon modes. The

energy of the perovskite can decrease by displacing the octahedra along these modes forming lower symmetry phases, which can occur when decreasing the temperature of the structure. The M-mode generates an in-phase tilt pattern, which means that the octahedra are tilted in the same orientation in every layer perpendicular to the direction of the mode. An illustration of the M-mode can be seen in Figure 2.2a. Looking at the structure in Figure 2.2b the R-mode instead generates an out-of-phase tilt pattern, which means that the octahedra are tilted in opposite orientation in the subsequent layer perpendicular to the direction of the mode [12].

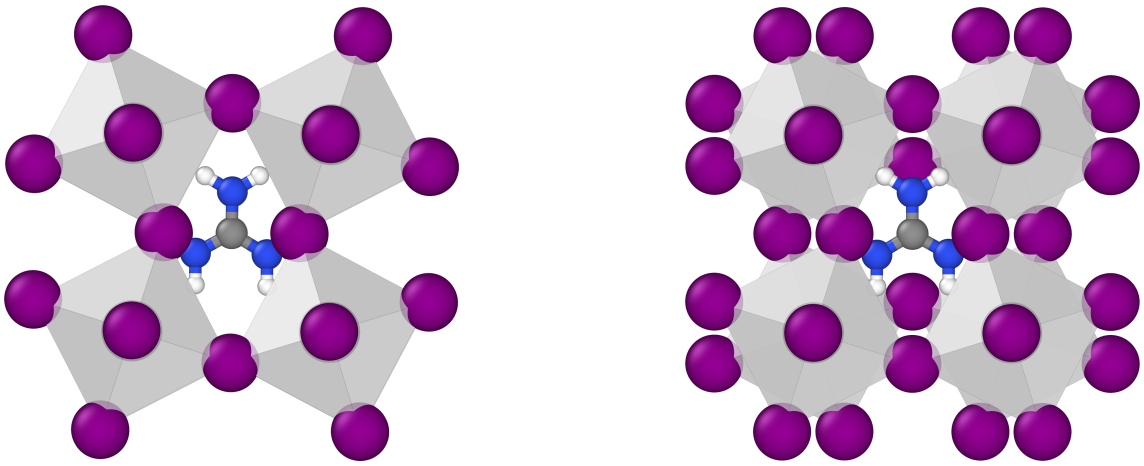

(a) In-phase tilt **(b)** Out-of-phase tilt

Figure 2.2: Comparison of perovskite structures with different tilts.

The phases arising from the tilt of the octahedra are commonly classified using the Glazer notation. If the structure exibits symmetry breaking resembling an in-phase tilt pattern it is represented with a plus sign, while a minus sign is used to represent out-of-phase tilt pattern. The amplitude of the tilt is represented through the letters $a - c$. If two cartesian directions have the same tilt pattern and amplitude they are represented by the same letter. For example $a^+b^-b^-$ means that the octahedra are tilted in-phase in one of the cartesian directions and out-of-phase in the other two. Here a and b correspond to different tilt amplitudes [13].
The preferred tilt patterns of the perovskite depends on the composition. A quantity commonly used to predict the ideal phase of a perovskite is the Goldschmidt's tolerance factor t:

$$t = \frac{r_A + r_X}{\sqrt{2}(r_B + r_X)}, \tag{2.1}$$

where r_A, r_B and r_X are the radius of the atoms or molecules occupying the A-, B- and X-site respectively. The model predicts that the perovskite will prefer a cubic phase for a tolerance factor between 0.9 and 1, a lower symmetry 3D perovskite phase between 0.71 and 0.9 and a non-perovskite phase outside of this range [14].
This metric can be useful for rough approximation of the phase. However, in the case of hybrid halide perovskites it can sometimes be inaccurate. The reason is both due to the lack of spherical symmetry in most molecules used in the A-site, including MA, FA and GUA, but more importantly the bonds formed between the octahedra and the hydrogen atoms of the molecules [15].

2.2 Guanidinium

Guanidinium is an organic molecule consisting of one carbon atom bonded to three NH_2-groups. The NH_2-groups are located in a plane and are evenly spaced around the carbon atom with a 120° separation as can be seen in Figure 2.3c. The geometry means that the molecule has a D_{3h} symmetry [16, 17, 18]. This symmetry causes the molecule to have zero dipole moment, which is one of the reasons it can have beneficial effects when included in hybrid halide perovskites. The lack of dipole moment reduces ion migration and hysteresis in current-voltage measurements, while increasing charge carrier life time. The second reason it has beneficial attributes for hybrid halide perovskites is the six hydrogen atoms, which can form bonds with the iodide in the lattice. The bonds increase the stability of the lattice [16, 19]. These two factors make GUA quite unique as an A-site candidate, since it combines the benefit of zero dipole moment that is usually only found in inorganic ions such as Cs with the benefit of hydrogen bonds that one gets from organic molecules.
The size of GUA, relative to MA and FA is also an important factor. It is significantly larger, which means that the hydrogen atoms are generally closer to the iodide atoms, creating stronger bonds [16]. However, it also results in a strain on the lattice, which according to the Goldsmith's tolerance factor would mean that GUAPI is not stable in a 3D perovskite state. Current experimental results agree with this statement, however as will be proven in this thesis, it is computationally possible to simulate a stable 3D perovskite phase for GUAPI.

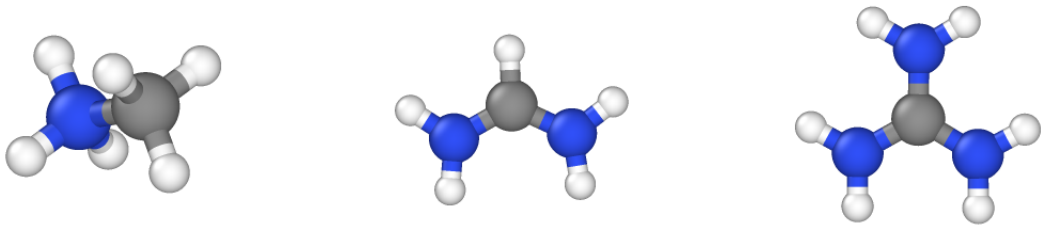

(a) Methylammonium **(b)** Formamidinium **(c)** Guanidinium

Figure 2.3: The organic molecules methylammonium (MA), formamidinium (FA) and guanidinium (GUA).

2.3 Morphotropic phase boundary

This thesis will investigate the mixing of the three materials mentioned above, which exhibit different phases. This can result in the coexistence of multiple phases in the lattice. The morphotropic phase boundary (MPB) refers to the composition at which the two phases are energetically equally favorable [20]. The coexistence of phases can result in patterns. An example is the mixing of MAPI and FAPI. Both tend to form tetragonal phases, however MAPI prefers the $a^0a^0c^-$ phase, while FAPI prefers the $a^0a^0c^+$ phase. It has been observed in previous computational studies that the pattern is dependent on the size of the system [9]. For instance for system sizes of the order of $\mathcal{O}(10^4) - \mathcal{O}(10^5)$ atoms the phases order in a layered pattern.

However, for system sizes of $\mathcal{O}(10^6)$ atoms the structure forms a twinning pattern. The twinning pattern consists of different layers with alternating preference for the direction of the mode.
There has not been many studies on how MPBs can be utilized in hybrid halide perovskites, however there are speculations that they could be useful in enhancing the performance of photovoltaic devices. For instance it is well known that the MPB in ferroelectric materials such as $PbZn_xTi_{1-x}O_3$ can be utilized to enhance piezoelectric and dielectric properties [9].

2.4 Solar cells

To understand the importance of the optoelectronic properties of the perovskite for producing high-efficiency solar cells, it is important to understand how a perovskite solar cell works. Solar cells can be fabricated in many ways, but the most common architecture for perovskite solar cells is to have a layered structure as can be seen in Figure 2.4. The middle layer consists of perovskite crystals and is called the active layer. When sunlight reaches this layer, electron-hole pairs are created through the excitation of electrons from the valence band to the conduction band. The active layer is sandwiched between the hole transport layer (HTL) and the electron transport layer (ETL), which transport holes and electrons, respectively, to the respective electrodes, while hindering the reverse process. The electrodes can then be connected to a circuit through which the produced electricity can be transferred.

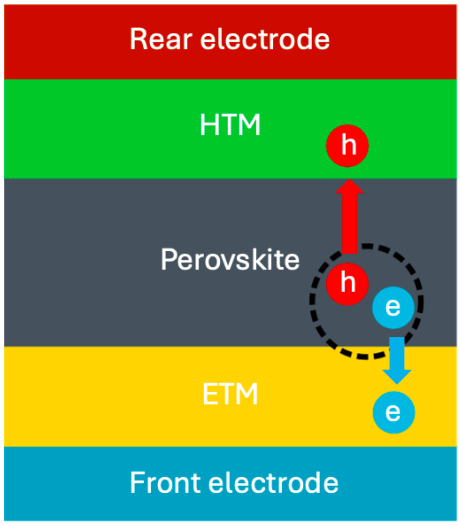

Figure 2.4: Perovskite solar cell architecture with an electron-hole pair being generated and subsequently separated.

To produce a high efficiency perovskite solar cell one of the most important properties of solar cells is the bandgap, which defines the energy difference between the highest energy site in the valence band and the lowest energy site in the conduction band. The power conversion efficiency (PCE) of a solar cell can be calculated as

$$PCE = \frac{J_{\mathrm{SC}} V_{\mathrm{OC}} FF}{P_{\mathrm{in}}}, \tag{2.2}$$

where P_{in} is the power of the incident photons. The short circuit current (J_{SC}), which is the maximum achievable current decreases exponentially with the bandgap. However, the open circuit voltage (V_{OC}), which is the maximum achievable voltage, increase linearly with the bandgap. The fill factor (FF) also increases with the bandgap. The fill factor takes into account the actual achievable maximum power, since J_{SC} and V_{OC} can't be achieved simultaneously. This results in an optimal bandgap determined by Shockley-Quiesser limit at 1.34 eV for the absorption of the solar spectrum [21].
By changing the composition of the halide perovskites, it is possible to tune the bandgap to get very close to this. Modifying the A-site cation is particularly efficient for this purpose. Hybrid halide perovskites are especially successful in achieving a bandgap close to the desired value, as the large size of the organic cations induces lattice distortions that significantly influence the band structure [22].
However, to achieve high efficiency solar cells it is also important to reduce the loss caused by recombination of the produced electron-hole pairs. The total loss depends on the fabrication of the entire solar cell and not just the active material. However, studies have shown that incorporating GUA into MAPI and FAPI perovskites could increase the charge carrier life-times, thus reducing the loss from recombination [5].

2.5 Density functional theory

In order to describe the behavior of a material in condensed matter physics, one usually views the material as a collection of N electrons and M ions [23]. The evolution of this system can be fully described by the Schrödinger equation

$$i\hbar\frac{\partial}{\partial t}\Psi(\mathbf{r}_1, \mathbf{r}_2, ..., \mathbf{r}_N; \mathbf{R}_1, \mathbf{R}_2, ..., \mathbf{R}_M, t) = \hat{H}\Psi(\mathbf{r}_1, \mathbf{r}_2, ..., \mathbf{r}_N; \mathbf{R}_1, \mathbf{R}_2, ..., \mathbf{R}_M, t), \quad (2.3)$$

where $\mathbf{r}_i$ are the positions of the electrons and $\mathbf{R}_j$ are the positions of the ions. The Hamiltonian can be decomposed into a kinetic term $\hat{T}$ and a potential term $\hat{V}$. The kinetic term can be further subdivided into one for the electrons and ions respectively

$$\hat{T} = -\sum_{i=1}^{N}\frac{\hbar^2}{2m_e}\nabla_i^2 - \sum_{I=1}^{M}\frac{\hbar^2}{2M_I}\nabla_I^2, \quad (2.4)$$

where m_e is the mass of the electron and M_I is the mass of the nuclei.
Meanwhile the potential energy landscape depends on the two repulsive interactions between ion-ion pairs and electron-electron pairs and the attractive interactions between ion-electron pairs

$$\hat{V} = \frac{1}{2}\sum_{i\neq j}\frac{1}{|\mathbf{r}_i - \mathbf{r}_j|} + \frac{1}{2}\sum_{I\neq J}\frac{Z_I Z_J}{|\mathbf{R}_I - \mathbf{R}_J|} - \sum_{i,I}\frac{Z_I}{|\mathbf{r}_i - \mathbf{R}_I|}, \quad (2.5)$$

where Z_I is the atomic number of nuclei I.
This is a $3(N + M)$ dimensional problem and would thus be computational unfeasible for larger systems. Even systems with only a few particles become prohibitively expensive without approximations. A method to reduce the complexity to a 3-dimensional problem, while still enabling accurate simulations is DFT. The

method only considers the ground-state of the system (there are extensions like time-dependent DFT that covers the excited states), thus the time-independent Schrödinger equation is sufficient, since the ground-state is time-independent for an isolated system

$$E\Psi(\mathbf{r}_1, \mathbf{r}_2, ..., \mathbf{r}_N; \mathbf{R}_1, \mathbf{R}_2, ..., \mathbf{R}_M) = \hat{H}\Psi(\mathbf{r}_1, \mathbf{r}_2, ..., \mathbf{r}_N; \mathbf{R}_1, \mathbf{R}_2, ..., \mathbf{R}_M). \tag{2.6}$$

2.5.1 Born-Oppenheimer approximation

Observing that the mass of the two kinds of particles (electrons and nuclei) in the system are of completely different magnitudes (the mass of a single proton is more than 1000 times the mass of an electron), the electrons move much faster than the nuclei. Any movement of the nuclei will thus result in an almost instantaneous (relative to the time scales of nucleus motion) response from the electrons. As a consequence, the total wavefunction can be expressed as a product of an electronic wave function ψ and a nuclear wave function χ.

$$\Psi(\mathbf{r}_1, \mathbf{r}_2, ..., \mathbf{r}_N; \mathbf{R}_1, \mathbf{R}_2, ..., \mathbf{R}_M) = \psi_{\mathbf{R}}(\mathbf{r}_1, \mathbf{r}_2, ..., \mathbf{r}_N)\chi(\mathbf{R}_1, \mathbf{R}_2, ..., \mathbf{R}_M). \tag{2.7}$$

Observe that the nuclear wave function only depends on the position of the nuclei, while the electronic wave function depends on both the position of nuclei and electrons. However, when isolating the electronic wavefunction these parameters can be seen as fixed, due to the slower motion of the nuclei. In this way, electronic and nuclear dynamics can be separated into the two following equations (observe that Hartree atomic units have been used to simplify the equations)

$$\left[-\sum_i \frac{\nabla_i^2}{2} + \sum_i V_n(\mathbf{r}_i; \mathbf{R}) + \frac{1}{2}\sum_{i \neq j} \frac{1}{|\mathbf{r}_i - \mathbf{r}_j|}\right] \psi_{\mathbf{R}} = E_{\mathbf{R}}\psi_{\mathbf{R}} \tag{2.8}$$

$$\left[-\sum_i \frac{\nabla_I^2}{2M_I} + \frac{1}{2}\sum_{I \neq J} \frac{Z_I Z_J}{|\mathbf{R}_I - \mathbf{R}_J|} + E_{\mathbf{R}}\right] \chi = E_{\text{tot}}\chi, \tag{2.9}$$

where $E_{\mathbf{R}}$ encodes the electronic effects inside the second equation. This separation breaks the problem of solving the Schrödinger equation into two steps. If one can solve equation (2.8) and obtain $E_{\mathbf{R}}$, then equation (2.9) can be solved subsequently. This in turn solves the full wavefunction Ψ of the system through equation (2.7).

2.5.2 Hohenberg-Kohn theorems

Fundamentally the formulation of DFT relies on the two Hohenberg-Kohn theorems [24].

Theorem 1: The external potential V_n is within a trivial additive constant a unique functional of the electron density $n(\mathbf{r})$.

Theorem 2: For a trivial density $\tilde{n}(\mathbf{r})$, which satisfies the necessary boundary conditions such as $\tilde{n}(\mathbf{r}) \geq 0$, $\int \tilde{n}(\mathbf{r})d\mathbf{r} = N$, it holds that $E[n_0] \leq E[\tilde{n}]$, where n_0 is

the ground-state energy density.

From the first theorem it follows that since the external potential is fully determined by the electron density, so is the full Hamiltonian in equation (2.8). The many-electron wavefunction can thus be fully determined by the ground-state electron density n_0 and as a consequence all the other properties of the system as well. This simplifies the initial problem of solving the many-body Schrödinger equation from a $3N$ dimensional problem to a 3 dimensional problem.
The next observation to make is that the energy for a many electron system can be expressed as a functional of the many-electron wave function

$$E = \langle\psi|\,\hat{H}\,|\psi\rangle = \int d\mathbf{r}_1 d\mathbf{r}_2..d\mathbf{r}_N \psi^*(\mathbf{r}_1, ..., \mathbf{r}_N)\hat{H}\psi(\mathbf{r}_1, ..., \mathbf{r}_N). \tag{2.10}$$

Since both the Hamiltonian and the wave function are determined by the electron density, it means that the energy is a functional of the electron density $E = E[n]$. According to the second theorem the ground-state electron density n_0 is the electron density for which this functional is minimized.

2.5.3 Kohn-Sham equation

The Hohenberg-Kohn theorems simplifies the many-body Schrödinger equation to a 3-dimensional problem by proposing that the energy of the system can be described by a functional of electron density. However, it does not explain how this functional can be constructed [23]. There is no precise solution and many good approximations have been made since the introduction of the theorems. Before applying any approximation we observe that the Hamiltonian in equation (2.10) is the one in the many-electron Schrödinger equation (2.8)

$$\hat{H} = -\sum_i \frac{\nabla_i^2}{2} + \sum_i V_n(\mathbf{r}_i; \mathbf{R}) + \frac{1}{2}\sum_{i\neq j} \frac{1}{|\mathbf{r}_i - \mathbf{r}_j|}. \tag{2.11}$$

The main issue of using this expression in equation (2.10) is the kinetic term, due to the interaction of the electrons.
A solution is to use the Kohn-Sham approach, which is based on the assumption that the interacting many-electron system can be replaced by a non-interacting system with an effective external potential that has the same ground-state energy. Under this assumption the many-electron wavefunction can be separated into a product of the single-electron wavefunctions ϕ_i

$$\psi(\mathbf{r}_1, ..., \mathbf{r}_N) = \phi_1(\mathbf{r}_1)...\phi_N(\mathbf{r}_N). \tag{2.12}$$

This expression is not sufficient for describing fermionic particles such as electrons, since it is not antisymmetric, however this can be fixed by using the Slater determinant. ϕ_i are usually denoted as Kohn-Sham orbitals to emphasize that they represent a fictitious system with the purpose of mathematically simplifying the problem of solving the many-body Schrödinger equation.

The separation of the many-electron wavefunction into a product of single-electron wavefunctions implies that the electron density can be expressed as a sum of their individual probabilities

$$n(\mathbf{r}) = \sum_i |\phi_i(\mathbf{r})|^2. \tag{2.13}$$

This relation can be utilized when replacing the many-electron wavefunction in the functional expression of the energy equation (2.10). However, an extra term will have to be introduced called the exchange-correlation energy $E_{\mathrm{XC}}[n]$ to compensate for the energy difference between an interacting and non-interacting system

$$E[n] = \overbrace{\underbrace{\int d\mathbf{r} n(\mathbf{r}) V_n(\mathbf{r};\mathbf{R})}_{\text{External potential}} - \underbrace{\sum_i \int d\mathbf{r} \phi_i^*(\mathbf{r}) \frac{\nabla^2}{2} \phi_i(\mathbf{r})}_{\text{Kinetic energy}} + \underbrace{\frac{1}{2} \iint d\mathbf{r} d\mathbf{r}' \frac{n(\mathbf{r}) n(\mathbf{r}')}{|\mathbf{r}-\mathbf{r}'|}}_{\text{Hartree energy}}}^{\text{Total energy in the independent electrons approximation}} + \underbrace{E_{\mathrm{XC}}[n]}_{\text{XC energy}}. \tag{2.14}$$

The reason it is called the exchange-correlation energy is due to that it is a sum of two different energy corrections compensating for two different physical phenomena. The exchange energy accounts for the Pauli exclusion principle preventing two electrons from occupying the same state. The correlation energy is due to the repulsive forces between electrons, resulting in a reduced probability of finding two electrons close to each other ($|\Psi(\mathbf{r}_1,\mathbf{r}_2)|^2 \leq |\phi_1(\mathbf{r}_1)\phi_2(\mathbf{r}_2)|^2$).
Now according to the second Hohenberg-Kohn theorem the ground-state electron density n_0 is the electron density for which the energy is minimized, thus by the variational principle it follows that

$$\left.\frac{\delta E[n]}{\delta n}\right|_{n_0} = 0. \tag{2.15}$$

Imposing the requirement that ϕ_i should be orthonormal while minimizing the energy with respect to the Kohn-Sham orbitals yields the Kohn-Sham equation

$$\left[-\frac{1}{2}\nabla^2 + V_n(\mathbf{r};\mathbf{R}) + \frac{1}{2}\int d\mathbf{r}' \frac{n(\mathbf{r}')}{|\mathbf{r}-\mathbf{r}'|} + V_{\mathrm{XC}}(\mathbf{r})\right]\phi_i(\mathbf{r}) = \epsilon_i \phi_i(\mathbf{r}). \tag{2.16}$$

V_{XC} is called the exchange-correlation potential and can be written as

$$V_{\mathrm{XC}}(\mathbf{r}) = \left.\frac{\delta E_{\mathrm{XC}}[n]}{\delta n}\right|_{n(\mathbf{r})}. \tag{2.17}$$

2.5.4 Self-consistency

The Kohn-Sham equation (2.16) is solved through a self-consistency loop. First, an initial guess is made for the ground-state electron density. This is inserted into the Kohn-Sham equation to find a solution for the Kohn-Sham orbitals. The actual electron density for this solution is then calculated using equation (2.13). If the difference between the solution and the initial guess is within a set threshold δ the algorithm has converged and a solution for the ground-state electron density has been found. Otherwise a new guess is made.

2.5.5 Exchange-correlation functionals

Choosing a reasonable exchange-correlation functional is crucial to achieve a reasonable result. The choice of the functional is usually a trade-off between accuracy and computational cost.
Many functionals have been developed over the years. One of the simplest is the local density approximation (LDA), which approximates that each electron experiences a homogeneous electron gas with the same local electron density. This can be formulated as:

$$E_{\mathrm{XC}}^{LDA}[n] = \int n(\mathbf{r})\epsilon_{\mathrm{XC}}(n(\mathbf{r}))d\mathbf{r}, \tag{2.18}$$

where ϵ_{XC} is the exchange-correlation energy per electron for a homogeneous electron gas.
A common refinement of LDA is to formulate the exchange-correlation energy that also depends on the gradient of the electron density

$$E_{\mathrm{XC}}^{GGA}[n] = \int n(\mathbf{r})\epsilon_{\mathrm{XC}}(n(\mathbf{r}), \nabla n(\mathbf{r}))d\mathbf{r}. \tag{2.19}$$

These kinds of functionals are called generalized gradient approximations (GGA). In this thesis a functional called SCAN+rVV10 is used, which is based on the strongly constrained and appropriately normed functional (SCAN) with an added correction (+rVV10) to improve the performance when describing van der Waals forces. SCAN and by extension SCAN+rVV10 is part of the family of meta-GGA functionals. The difference to regular GGA is that exchange-correlation energy also depends on the kinetic energy density [25].

2.6 Molecular dynamics

The dynamics of a structure can be simulated by moving the atoms according to a forcefield. This can be used to calculate thermodynamic properties of the material. This requires that the material is first equilibrated. Once in equilibrium the material needs to be sampled during a long enough time to reduce statistical noise. To reduce statistical noise, it is also important that the system is large enough. By sampling the positions and velocities of the particles it is possible to calculate thermodynamic properties of the material [26].
The forces can be derived from a potential energy surface (PES) U of the system, which can be defined as

$$U = \sum_i U_i, \tag{2.20}$$

where $U_i = U_i(\{\mathbf{r}_{ij}\})$ is the potential energy of atom i, with $\mathbf{r}_{ij}$ being the relative position between atom i and j. A cutoff radius is used such that one only considers atom pairs with distances smaller or equal to the cutoff radius [27].
A general force expression for atom i can then be expressed as

$$\mathbf{F}_i = \sum_{i \neq j} \mathbf{F}_{ij}, \tag{2.21}$$

where

$$\mathbf{F}_{ij} = -\mathbf{F}_{ji} = \frac{\partial U_i}{\partial r_{ij}} - \frac{\partial U_j}{\partial r_{ji}}. \tag{2.22}$$

$\mathbf{F}_{ij}$ is the force acting from atom j on atom i, which can be influenced by other atoms.
By integrating Newton's equation of motion for instance through the Verlet algorithm the new positions of the particles can be calculated as

$$\mathbf{r}_i(t + \Delta t) \approx 2\mathbf{r}_i(t) - \mathbf{r}_i(t - \Delta t) + \frac{\mathbf{F}_i(t)}{m}(\Delta t)^2. \tag{2.23}$$

The error of this calculation is of the order of $\mathcal{O}(\Delta t^4)$ and is thus deemed one of the more accurate and at the same time easiest algorithms to use in MD simulations [26].
However, in the GPUMD package [7], which is utilized in this thesis to perform MD simulations, the velocity Verlet algorithm is used instead. It is quite similar, however it relies on calculating both the position and velocity of every particle as a function of time using the following pair of equations

$$\begin{cases} \mathbf{v}_i(t + \Delta t) \approx \mathbf{v}_i(t) + \dfrac{\mathbf{F}_i(t) + \mathbf{F}_i(t + \Delta t)}{2m_i}\Delta t \\ \mathbf{r}_i(t + \Delta t) \approx \mathbf{r}_i(t) + \mathbf{v}_i(t)\Delta t + \dfrac{1}{2}\dfrac{\mathbf{F}_i(t)}{m_i}(\Delta t)^2. \end{cases} \tag{2.24}$$

This process simulates an NVE ensemble (micro-canonical), since the number of particle N, the volume V and the energy E are conserved. However, in most practical situations other ensembles are of more interest. This is due to that the NVE ensemble describes an isolated system, which does not interact with its surrounding. An ensemble that will be used extensively in this thesis to simulate realistic phase transitions during heating and cooling trajectories of materials is the NpT ensemble, which conserves the number of particles N, the pressure p and the temperature T, which can be achieved through the use of different thermostats and barostats that regulates the coupling to an external heat bath and pressure bath respectively. The thermostat used in this thesis is the Berendsen thermostat, which scales the velocities of atoms in the system as follows

$$\mathbf{v}_i^{\text{scaled}} = \mathbf{v}_i\sqrt{1 + \frac{\Delta t}{\tau_T}\left(\frac{T_0}{T} - 1\right)}, \tag{2.25}$$

with τ_T being the coupling time, T_0 the target temperature and T is the current temperature.
The barostat that will be used is the stochastic cell rescaling barostat, which is an extension of the Berendsen barostat. In case all three directions are coupled the Berendsen barostat scales the simulation box matrix A and the position of the atoms $\mathbf{r}_i$ using a scaling matrix M, such that

$$\begin{cases} A^{\text{scaled}} = MA \\ \mathbf{r}_i^{\text{scaled}} = M\mathbf{r}_i. \end{cases} \tag{2.26}$$

The components of M are defined as

$$M_{\alpha\beta} = 1 - \frac{\gamma_{\alpha\beta}\Delta t}{3\tau_p}(p_{\alpha\beta}^{\text{target}} - p_{\alpha\beta}^{\text{current}}), \tag{2.27}$$

where $\gamma_{\alpha\beta}$ is the isothermal compressibility, τ_p is the pressure coupling time, $p_{\alpha\beta}^{\text{target}}$ is the target pressure and $p_{\alpha\beta}^{\text{current}}$ is the current pressure.
The stochastic cell rescaling barostat further adds a stochastic term

$$M_{\alpha\beta}^{\text{stochastic}} = \sqrt{\frac{1}{D_{\text{couple}}}}\sqrt{\frac{\gamma_{\alpha\beta}\Delta t}{3\tau_p}\frac{2k_B T^{\text{target}}}{V}}R_{\alpha\beta}, \tag{2.28}$$

where T^{target} is the target temperature, V is the current volume of the system, $R_{\alpha\beta}$ are numbers drawn from a Gaussian distribution with mean zero and the variance one and D_{couple} are the number of coupled direction [26].

2.7 Neuro-evolution potential

There are many ways to obtain a PES that can be used for MD. One method is to train a neuro-evolution potential, which is what was mostly used in this thesis. The advantage of this approach is that one can train the model on DFT data and thus achieve a similar accuracy, while not requiring to explicitly use DFT to calculate the forces at every frame in the MD simulation. DFT calculations on large structures of a few 10 000 atoms would be computationally infeasible. Instead the training structures used are usually only a few hundred atoms, for which DFT is a more reasonable tool. Since the simulation cells used in MD simulations are usually different kinds of replications of the smaller training cells, it is generally enough for the model to only be trained on the small structures.
A neuro-evolution potential is a machine learning (ML) architecture, which unlike many ML models does not rely on gradient descent to find the optimal solution. Instead it uses evolutionary algorithms, which are global search approaches and thus generally avoids the issue of getting stuck in local minima, which gradient descent methods usually struggles with. However these methods are usually more computationally demanding since it requires the evaluation of the loss function multiple times in every generation. The process is thus usually accelerated via GPU using the GPUMD package [27].
The NEP model is based on a feed forward neural network. The input layer consists of descriptor vectors q_ν^i ($1 \leq \nu \leq N_{\text{des}}$), which encode the surrounding of each atom i, while the output layer is the site energy U_i. There can be many hidden layers, but the implementation in the GPUMD package uses only one [7]. The state of the hidden layer can be represented by x_μ ($1 \leq \mu \leq N_{neu}$), where N_{neu} is the number of neurons in the hidden layer. One can then define the state of the hidden layer as

$$x_\mu = \tanh\left(\sum_{\nu=1}^{N_{des}} w_{\mu\nu}^{(1)} q_\nu^i - b_\mu^{(1)}\right), \tag{2.29}$$

where $w_{\mu\nu}^{(1)}$ is the connection weight between the neurons x_μ and q_ν^i, and $b_\mu^{(1)}$ is the bias for the neuron x_μ.

The output layer is then calculated as

$$U_i = \sum_{\mu=1}^{N_{neu}} w_\mu^{(2)} x_\mu - b^{(2)}, \tag{2.30}$$

where $w_\mu^{(2)}$ is the connection weight between the neuron U_i and x_μ, and $b^{(2)}$ is the bias for the neuron U_i.
When training the neural network one tries to determine optimal values for the weights and biases to minimize a loss function. The loss function is a quantification of the error between the predicted forces, virials and energies by the ML model and the training data. One can define a vector $\mathbf{z}$ of dimension N_{par}, i.e. the number of parameters in the neural network. The problem is thus to find the real-valued solution to

$$\mathbf{z}^* = \underset{\mathbf{z}}{\operatorname{argmin}} \quad L(\mathbf{z}), \tag{2.31}$$

where $L(\mathbf{z})$ is the loss function. The loss function is defined as the weighted sum of the energy, force, virial errors as well as $\mathcal{L}_1$ and $\mathcal{L}_2$ regularization loss function,

$$L(\mathbf{z}) = \lambda_e L_e(\mathbf{z}) + \lambda_f L_f(\mathbf{z}) + \lambda_v L_v(\mathbf{z}) + \lambda_1 L_1(\mathbf{z}) + \lambda_2 L_2(\mathbf{z}). \tag{2.32}$$

The energy loss function is defined as

$$L_e(\mathbf{z}) = \left(\frac{1}{N_{\text{str}}} \sum_{n=1}^{N_{\text{str}}} (U^{\text{NEP}}(n, \mathbf{z}) - U^{\text{tar}}(n))^2 \right)^{1/2}, \tag{2.33}$$

where N_{str} is the total number of structures in the training data set, $U^{\text{tar}}(n)$ is the target per-atom energy of the nth structure, and $U^{\text{NEP}}(n, \mathbf{z})$ is the corresponding energy calculated using the NEP potential with parameters $\mathbf{z}$. The force loss is defined as

$$L_f(\mathbf{z}) = \left(\frac{1}{3N} \sum_{i=1}^{N} (\mathbf{F}_i^{\text{NEP}}(\mathbf{z}) - \mathbf{F}_i^{\text{tar}})^2 \right)^{1/2}, \tag{2.34}$$

where N is the total number of atoms in the training data set and $\mathbf{F}_i^{\text{tar}}$ and $\mathbf{F}_i^{\text{NEP}}$ are the target force of the ith atom and that calculated from the NEP potential with the parameters $\mathbf{z}$.
The virial loss function is defined as

$$L_v(\mathbf{z}) = \left(\frac{1}{6N_{\text{str}}} \sum_{n=1}^{N_{\text{str}}} \sum_{\mu\nu} \left(W_{\mu\nu}^{\text{NEP}}(n, \mathbf{z}) - W_{\mu\nu}^{\text{tar}}(n) \right)^2 \right)^{1/2}, \tag{2.35}$$

where $W_{\mu\nu}^{\text{tar}}(n)$ and $W_{\mu\nu}^{\text{NEP}}(n, \mathbf{z})$ are the target per-atom virial $\mu\nu$ tensor component of the nth structure and that calculated from the NEP potential with parameter $\mathbf{z}$. The L_1 and L_2 loss are constructed based on the $\mathcal{L}_1$ and $\mathcal{L}_2$ norms of the parameter vector $\mathbf{z}$ as follows

$$\begin{cases} L_1(\mathbf{z}) = \dfrac{1}{N_{\text{par}}} \sum_{n=1}^{N_{\text{par}}} |z_n| \\ L_2(\mathbf{z}) = \left(\dfrac{1}{N_{\text{par}}} \sum_{n=1}^{N_{\text{par}}} z_n^2 \right)^{1/2}. \end{cases} \tag{2.36}$$

These two losses are useful in order to prevent overfitting. $L_1(\mathbf{z})$ tends to make the feature selection of the model sparse by setting less important features to zero. Meanwhile $L_2(\mathbf{z})$ only drives the less important features close to zero.
The minimization of the loss function is found through a separable natural evolution algorithm, since their complexity increases linearly with the number of fitting parameters [27]. Initially a population of solutions $\mathbf{z}$ are sampled from a Gaussian distribution with mean $\boldsymbol{\mu}$ and standard deviation $\boldsymbol{\sigma}$ [28]. This can be represented through

$$\mathbf{z}_k = \boldsymbol{\mu} + \boldsymbol{\sigma}\mathbf{s}_k, \tag{2.37}$$

where $\mathbf{s}_k$ is a value drawn from a Gaussian distribution $\mathcal{N}(0, \mathbb{I})$. The loss function is then evaluated for each individual solution and ranked from smallest to largest. The natural gradient can then be calculated by weighting the solutions with the weights u_k, such that individuals with smaller loss have a larger contribution

$$\begin{cases} \nabla_\mu J = \sum_{k=1}^{N_{\text{pop}}} u_k \mathbf{s}_k \\ \nabla_\sigma J = \sum_{k=1}^{N_{\text{pop}}} u_k (\mathbf{s}_k^2 - 1). \end{cases} \tag{2.38}$$

Lastly, these gradients are used to evolve the distribution of the population

$$\begin{cases} \boldsymbol{\mu} \leftarrow \boldsymbol{\mu} + \eta_{\boldsymbol{\mu}} \cdot \boldsymbol{\sigma} \cdot \nabla_\mu J \\ \boldsymbol{\sigma} \leftarrow \boldsymbol{\sigma} \cdot \exp(\eta_{\boldsymbol{\sigma}}/2 \cdot \nabla_\sigma J), \end{cases} \tag{2.39}$$

where η_μ and η_σ are the learning rates for the mean and standard deviation of the solution population respectively. This process constitutes one generation. The process in then repeated for multiple generations in order to train the neural network.

2.8 Machine-learned atomic cluster expansion

MACE potentials are a type of machine learning potentials that uses an equivariant message passing neural network to simulate the interaction between atoms, by representing each atom as a node in the network and the edges represent the interactions between atoms [29]. The features of each node are described by breaking the structure into clusters of atoms that can be used to describe the surrounding of each atom. What makes the architecture special compared to similar architectures like atomic cluster expansion (ACE) is that it uses high-order bodied features (4-body features) in every level and thus only two hidden layers are sufficient to create a quite accurate potential, but it has the drawback of being more computationally heavy than NEP-models. One example is MACE-MP-0, which is a model trained on 150 000 inorganic crystals. It can thus be used as a starting model when investigating a new material, which is what it is used for in this thesis [8].

2.9 Methodology

The project was divided into two main parts. First a NEP-model for pure GUAPI had to be trained. Once a stable and accurate model had been achieved, it could

be further trained on mixed (MA,FA,GUA)PbI_3 systems in order to achieve a NEP-model for the mixed perovskites. The reason is that the behavior of MAPI, FAPI and mixed (MA,FA)PbI_3 systems has been more explored. It is thus important to first achieve an accurate model for pure GUAPI since the validity of the model will be solely based on it's accuracy relative to DFT as well as physical reasonability. Furthermore, mixing will introduce further complexity into the behavior of the system. It is thus important to make sure that the model first can capture the behavior of the pure material.

2.9.1 Training NEP-model for pure GUAPI

The NEP-model for pure GUAPI was trained through a supervised active learning algorithm seen in Figure 2.5, which will be described in more detail in the following subsections.

2.9.1.1 Generating initial training structures

In order to train the NEP model an initial set of training structures had to be sampled. These structures should be representative of a material at relevant environmental conditions. This is so that the model can learn to recognise the patterns of the structure to make valid predictions of the optimal behavior at different conditions.
The initial structures can be generated through different methods. Generally a good starting point is to find an initial structure of the material based on experimental data. In the case of perovskites, a cubic structure is usually a good starting point since it is the natural phase of most 3D perovskite at sufficiently high temperatures. Additionally, it can be easily distorted into other configurations.
To generate more structures, one of the simpler methods is to apply artificial distortions, either based on known phonon modes or randomly generated with physical constrains, for instance through Monte Carlo sampling.
Another approach is to utilize previous models for the material. In the case of GUAPI no previous model was accessible, however a general model MACE-MP-0 could be used to generate physically reasonable structures.
Both of these methods were used to generate the initial GUAPI structures with an emphasize on the second method, since it tends to generate more physically reasonable structures.

2.9.1.2 Labeling training data through DFT

When the initial training structures had been generated the next step was to calculate the properties such as potential energy, forces and virial of the structures using DFT. DFT was performed using the VASP package with the SCAN+rVV10 functional. This functional was chosen due to previous studies highlighting its performance for DFT calculations of perovskites.
The process of calculating physical properties of the training structures using DFT is equivalent to labeling the training data in a typical supervised learning algorithm.

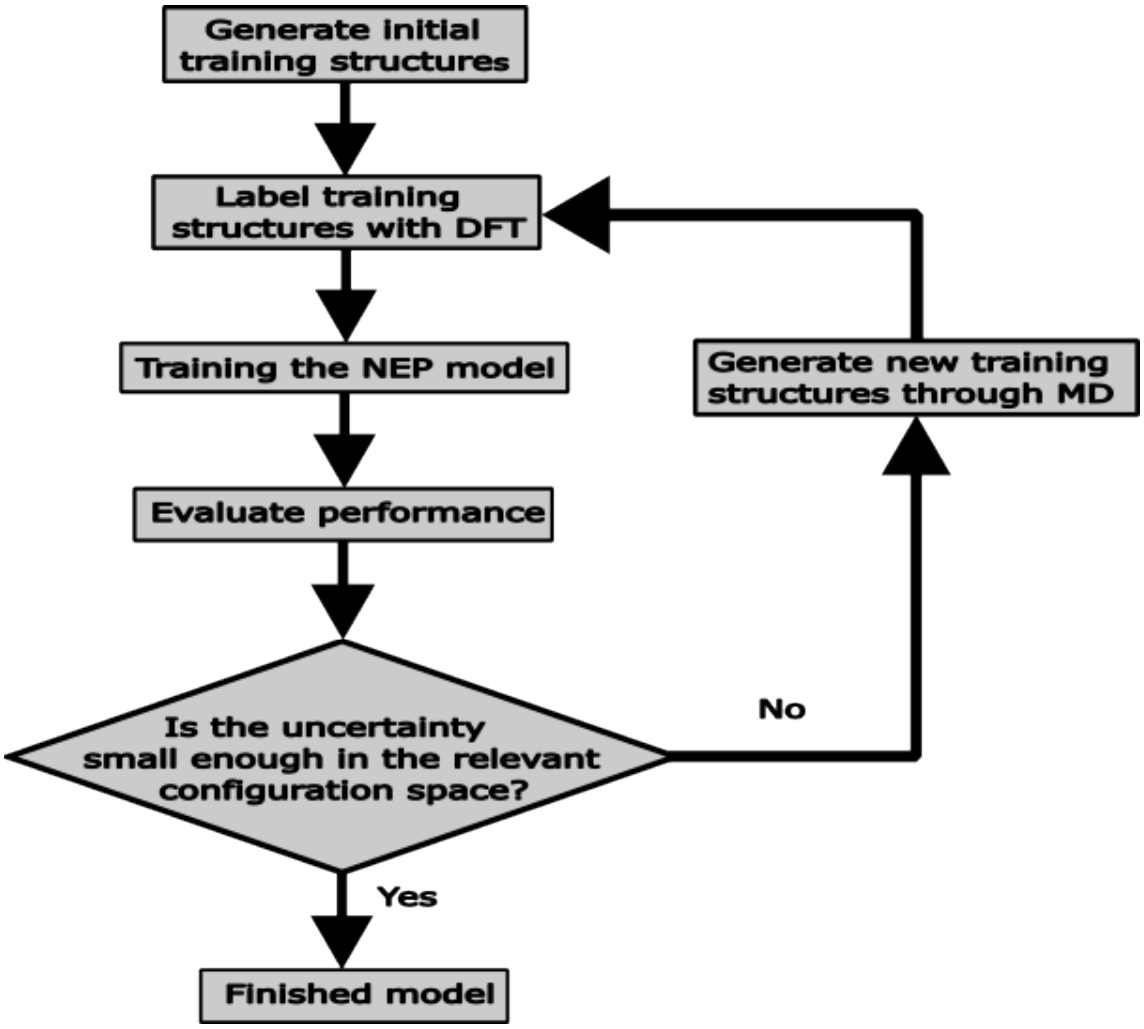

Figure 2.5: Process of training a NEP-model through supervised active learning.

2.9.1.3 Training and evaluating the NEP-model

Once the training structures had been labeled, the next step was to train the model. The model was trained using the GPUMD package. A set of initial hyper parameters was applied based on previous NEP-models for hybrid halide perovskites, which could then be adjusted in case the model did not perform well. 6 separate models were trained by dividing the training data into 5 batches of equal size. For each model one batch was used as test data and the rest as training data, except for the sixth model where the entire dataset was used as training data. The model without test data will be referred to as the full model, while the other models are referred to as split models. The purpose of the split models were to evaluate the performance of the model design and training data, while the full model was used as the actual model.

The performance of the model was tested with multiple methods. First, the loss and root mean square error (RMSE) of the models were calculated. Observing the train and test RMSE of the split models it was possible to detect if the model design was able to generate split models that could accurately capture the features of the entire

dataset without overtraining. This would be a sign that the full model also could generalise to similar structures that would appear during MD simulations.
Another method used was uncertainty analysis. New structures could be generated through MD simulations of the training data by applying the full NEP model. By simulating relevant environmental conditions it could be seen whether the model design was able to simulate these structures in a consistent and stable manner. This could be quantified by analysing the standard deviation of energy and forces predicted by the split models. If the standard deviation for a specific structure and environmental condition was large it was a sign that the model could not generalise well to that case.
By identifying the regions of the relevant configuration space were the model predictions had high uncertainty it was possible to employ an active learning algorithm to improve the model. This was done by further sampling the regions with high uncertainty by performing MD simulations in these regions. The structures generated from the MD simulations were then labeled using DFT and added to the training data. The model was then retrained and the process was repeated.

2.9.2 Training NEP-model for mixed (MA,FA,GUA)PbI_3

When a stable and accurate model for GUAPI had been trained, the model could be extended to mixed (MA,FA,GUA)PbI_3 systems. The training data for pure MAPI, FAPI and mixed (MA,FA)PbI_3 were reused from a previous NEP-model for mixed (MA,FA)PbI_3 systems. Mixed training structures containing GUA were created by replacing the molecule in the *A*-site of pure MAPI, FAPI and GUAPI structures. This was done for a diverse range of concentrations between the three materials. Both random distributions as well as deterministic patterns were used when replacing the molecules to cover a large region of configuration space. MD simulations of the training structures were then performed using the GUAPI NEP-model to generate more training structures. The general training procedure was otherwise the same as for the pure GUAPI model.

3
Results

3.1 Model performance

3.1.1 Loss and RMSE

To evaluate the performance of the final model one of the first metrics to evaluate is the loss and RMSE for both train and test data.
Figure 3.1 shows that the total loss decreased to an order of 10^{-1} at the end of training, which is quite typical for a well trained NEP model for a hybrid halide perovskite. The L_1 and L_2 loss terms follow the same trend, which suggests that overtraining is hampered. Looking at the bottom graph of Figure 3.1, the train RMSE mostly mirrors the behavior of the loss function, since by the definition of the energy, virial and force loss functions in a NEP-model from equation (2.33)-(2.35), they correspond to the RMSE of these properties.
Both the loss and RMSE plateau around 3×10^5 generations, which indicates that the model has converged and will not be improved by further training.

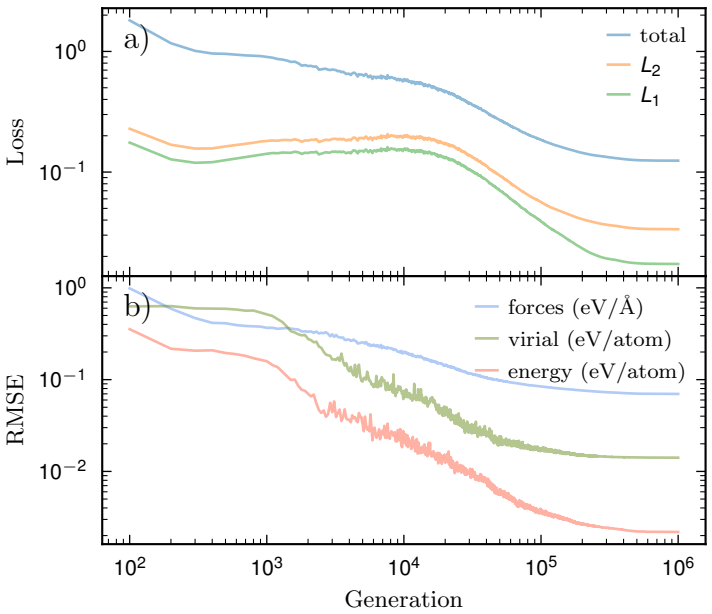

Figure 3.1: The upper image shows the loss for the training of the full model. The bottom image shows the training RMSE for forces, virial and energy of the full model.

3.1.2 Parity

Since the full NEP-model has no test data, the analysis of Figure 3.1 is insufficient to disclose the possibility of overfitting.
To verify the predictive performance of the full model, structures of varying size, composition and temperature were used as test structures. The forces and energies of the test structures were calculated with DFT and compared with the prediction of the NEP-model. The energy parity plot in Figure 3.2 shows that the test RMSE is of the same magnitude as the training RMSE, which means that the model can generalize to unseen data and is not overtrained. The statement can be further reinforced through the force RMSE in Figure 3.3, which is also of the same order as the train force RMSE.

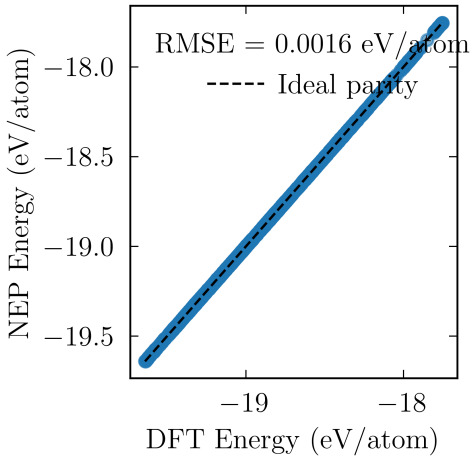

Figure 3.2: Energy parity plot of the test data.

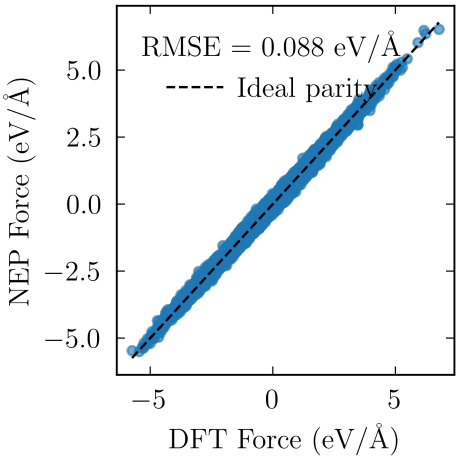

Figure 3.3: Force parity plot of the test data.

3.2 MAPI and FAPI systems

The purpose of the NEP-model is to be able to predict phase changes in $(\mathrm{MA}, \mathrm{FA}, \mathrm{GUA})\mathrm{PbI}_3$ systems. However, that implies that the model first should be able to predict the behaviors of the pure materials. Studying the phase behaviors of materials require large systems with over 10 000 atoms, which as previously mentioned is computationally unfeasible with DFT. Evaluating the performance of the NEP-model will instead have to be based on comparison with previous experimental and computational results.

3.2.1 MAPI MD simulations

The phase behavior of MAPI was investigated through heating and cooling MD simulations using the NpT ensemble. From previous studies it has been found that the ground-state of MAPI is the orthorhombic phase $a^-a^-c^+$ [12, 30, 31]. First

the ground-state was heated from 1 K to 400 K. This was done for a $16 \times 16 \times 16$ repetition of the unit cell with a heating rate of 7 K/ns.

To investigate the phase transitions three metrics were used. The potential energy and lattice parameters of the crystal are two metrics that are useful to observe the phase transitions in crystals, since they generally show a change during phase transitions. However, to more easily detect the phase transitions the heat capacity C_p was also investigated as:

$$C_p = \left(\frac{\partial U}{\partial T}\right)_p + p\left(\frac{\partial V}{\partial T}\right)_p . \tag{3.1}$$

In Figure 3.4 all three quantities show clear shifts at 190 K and 390 K, which are signs of phase transitions.

To identify the exact phases according to the Glazer notation a more thorough investigation of the structure had to be made. This was done by projecting the deviation of the lattice from the cubic structure $\mathbf{u}_i$ onto the M- and R-mode eigenvectors $\mathbf{e}_{ai}$ for each mode a and atom i. The projection $Q_a = \sum_i \mathbf{u}_i \cdot \mathbf{e}_{ai}$ was plotted for each mode in Figure 3.5 against temperature during the heating simulation. Below 190 K, the two R-modes are activated and one M-mode. This is in agreement with the ground-state being the orthorhombic $a^-a^-c^+$ phase. Between 190 K and 390 K only one R-mode is activated on average, which shows that the system is in the tetragonal $a^0a^0c^-$ phase. Above 390 K no mode is activated on average, which mean that the system is in the cubic $a^0a^0a^0$ phase. The change of activated modes is very sharp both at the orthorhombic to tetragonal phase and the tetragonal to cubic indicating first-order transitions. These results are in agreement with previous experimental and computational results [12, 30, 31, 32].

The cubic structure achieved from the heating simulation was subsequently cooled back to 1 K. The cubic to tetragonal phase transition occurs with almost no hysteresis as can be seen in Figure 3.4. However, the tetragonal to orthorhombic transition is notably absent during the cooling simulation. Previous computational studies using GPUMD have shown that this transition is hard to achieve during cooling simulations in part due to the energy barrier as can be seen during the heating simulation in Figure 3.4, but also because of its first-order nature [9, 32]. It is further confirmed by observing the activated modes during the cooling simulation in Figure 3.6 that the structures remains in the meta-stable tetragonal $a^0a^0c^-$ phase below 190 K instead of returning to the true ground-state. These simulations reproduced the phase transitions in pure MAPI validating the model's performance.

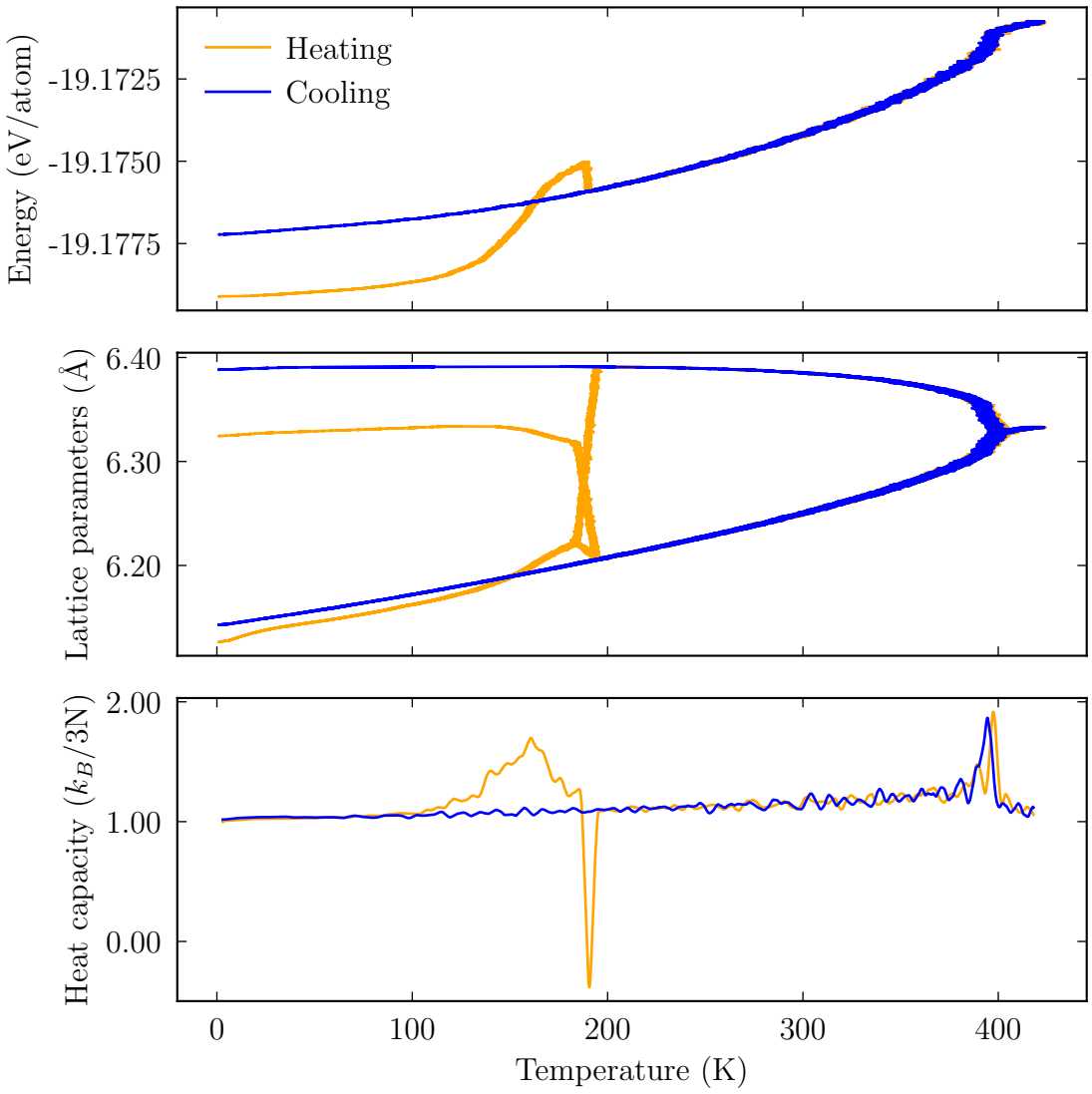

Figure 3.4: Potential energy, lattice parameters and heat capacity as a function of temperature of MAPI.

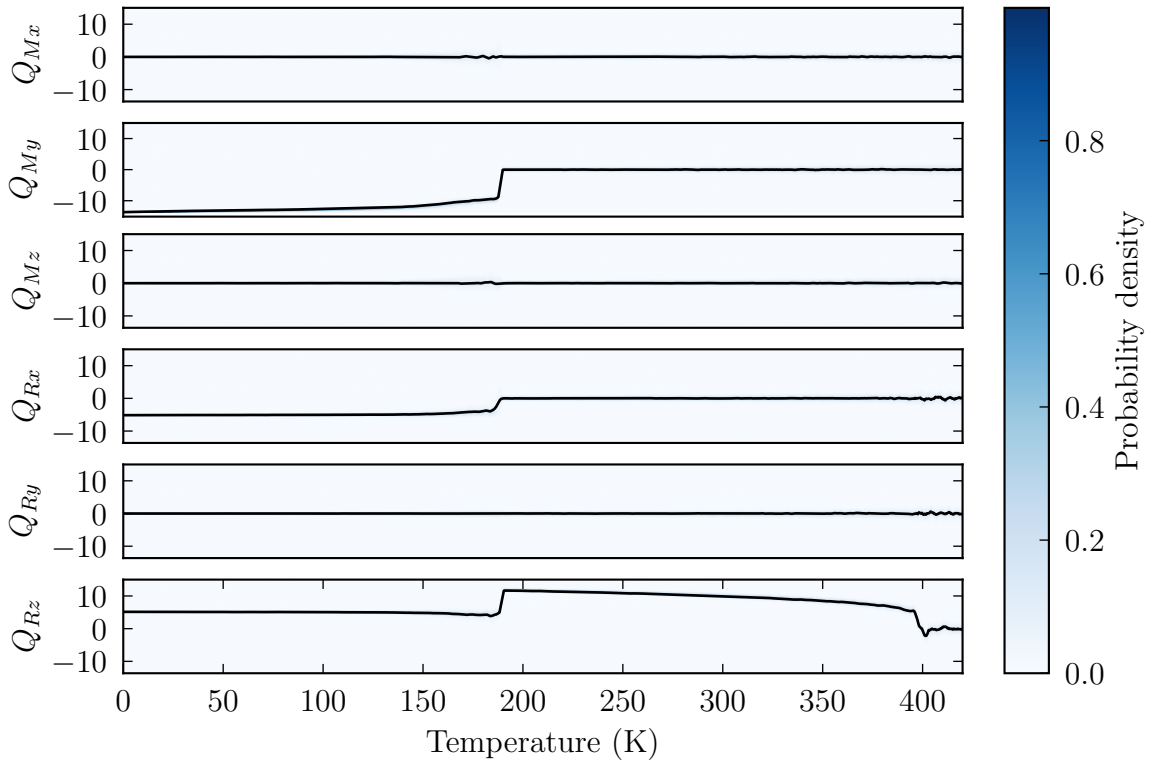

Figure 3.5: Mode projection of MAPI during heating simulation starting from the ground-state ($a^{-}a^{-}c^{+}$). The average mode projection is represented as a black line. Q_A represents the normalized amplitude of mode A.

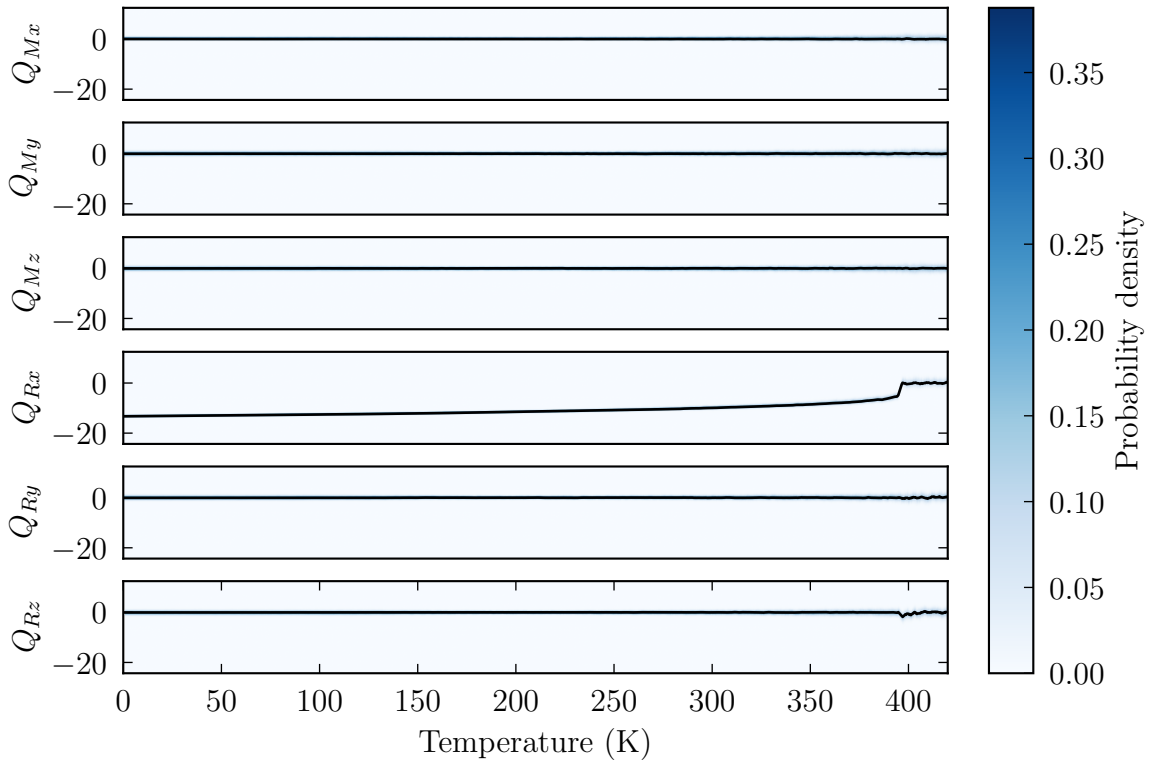

Figure 3.6: Mode projection of MAPI during cooling simulation starting from the the cubic phase ($a^0a^0a^0$). The average mode projection is represented as a black line.

3.2.2 FAPI MD simulations

The model's performance for FAPI was investigated in the same way as for MAPI. From a previous study it has been shown that the ground-state of FAPI is $a^-b^-b^-$ [33]. Investigating the potential energy, lattice parameters and heat capacity during a heating simulation from 1 K to 400 K with a heating rate of 7 K/ns of a $16 \times 16 \times 16$ repetition of the unitcell of the ground-state revealed a transition at 200 K and a second phase transition at 350 K. This can be seen in Figure 3.7. According to the activated modes in Figure 3.8 the first phase transition seems to be from $a^-b^-b^-$ to the tetragonal $a^0a^0c^+$ phase, while the second phase transition is to the cubic $a^0a^0a^0$ phase. The transition from the ground-state to the tetragonal phase seems to be of first-order due to the sharp shift of the mode activations, while the tetragonal to cubic phase transition seems to be continuous. This is in agreement with previous studies [33, 9].

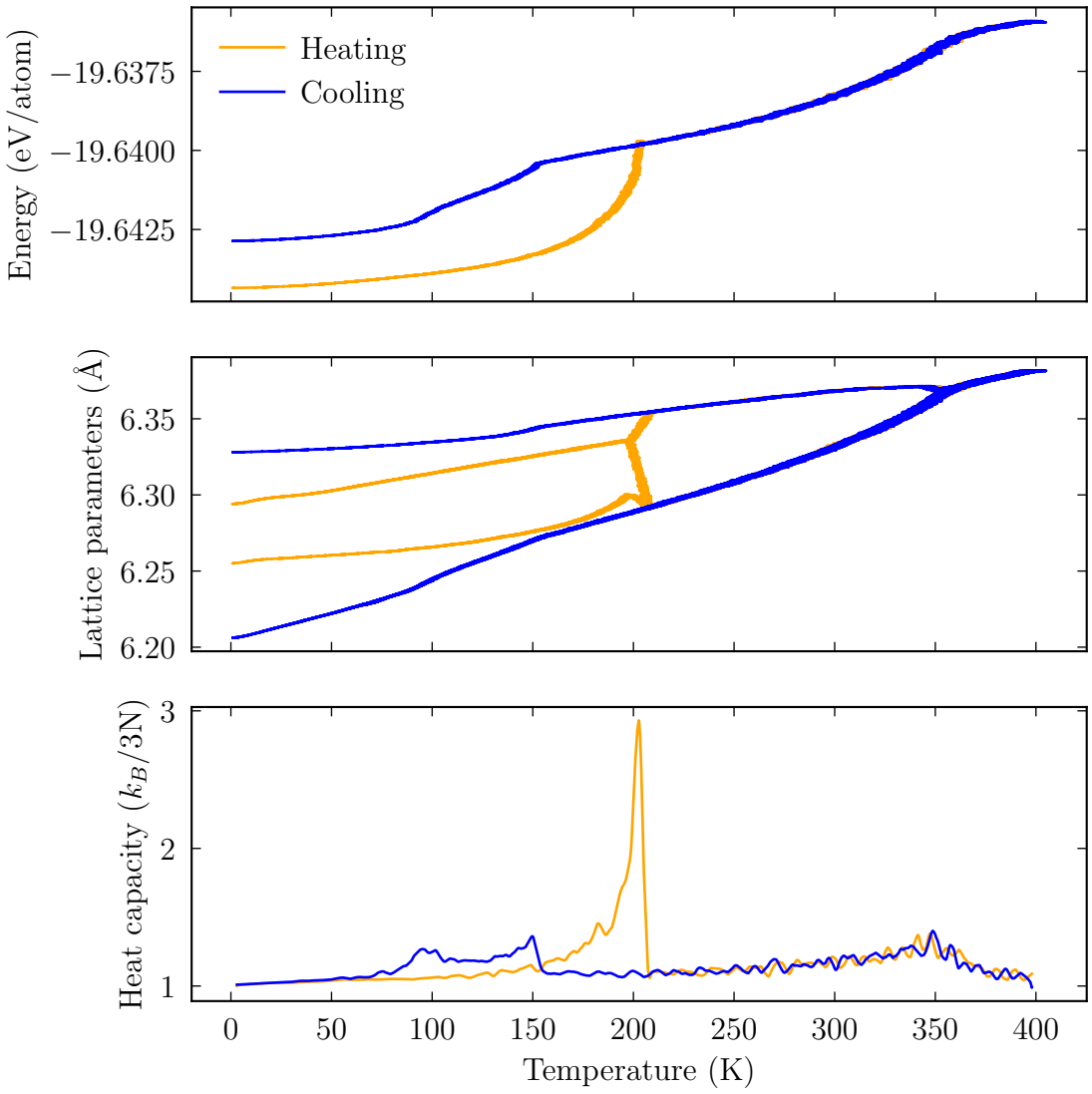

Figure 3.7: Potential energy, lattice parameters and heat capacity as a function of temperature of FAPI.

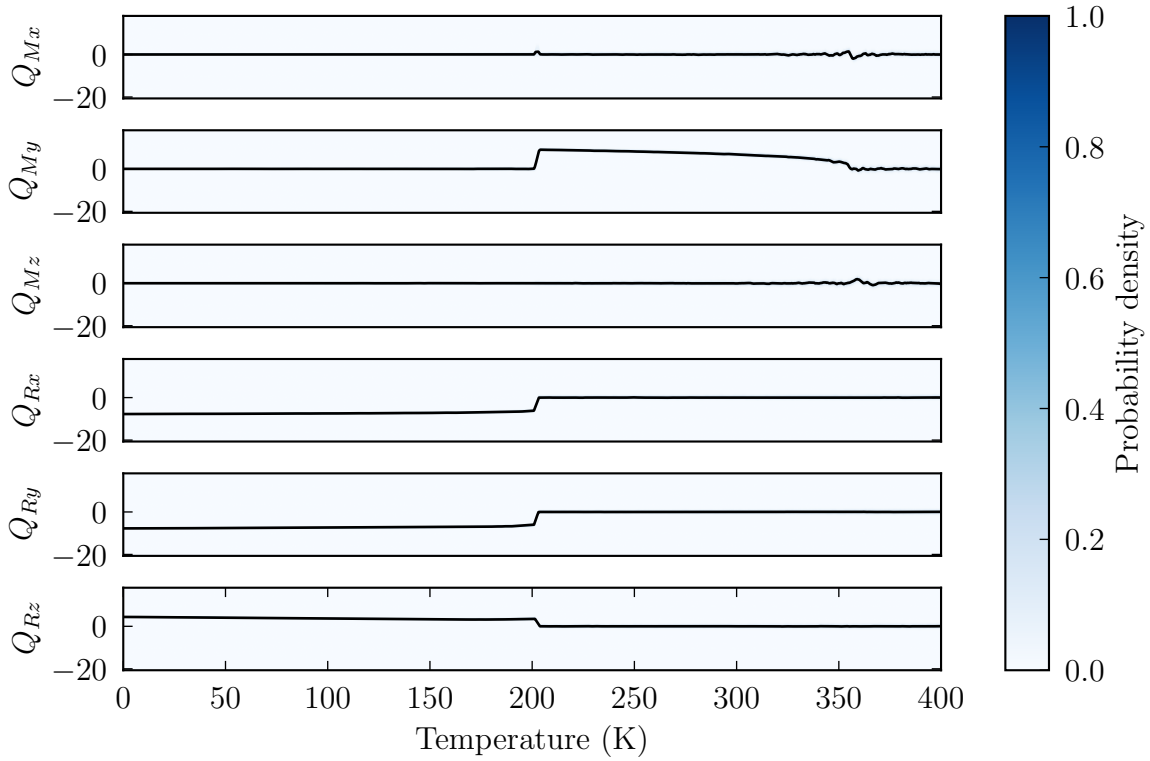

Figure 3.8: Mode projection of FAPI during heating simulation starting from the ground-state ($a^-b^-b^-$). The average mode projection is represented as a black line.

To observe the behavior of FAPI during a cooling simulation, the same method was used as for MAPI. The cubic phase achieved after the heating simulation was cooled from 400 K back to 1 K. Observing the difference between the heating and cooling simulation in Figure 3.7 the cubic to tetragonal phase transition had almost no hysteresis owing to its continuous nature. On the contrary the transition from the tetragonal phase to the ground-state around 200 K did not occur, but instead another phase transition around 150 K was found. Analysing the activated modes in Figure 3.9 a second phase transition can be identified. This phase transitions is from the tetragonal $a^0a^0c^+$ phase to orthorhombic $a^-a^-c^+$. This shows that the system does not return to the ground-state, but instead is stuck in a meta stable state. However, it is interesting that two peaks can be seen when observing the heat capacity during the transition from $a^0a^0c^+$ to $a^-a^-c^+$. This seems to be due to a delay between the dynamics of the lattice and the molecules. At the first peak around 150 K the lattice transitions to the $a^-a^-c^+$ phase, but the FA molecules are still oriented in the pattern associated with the $a^0a^0c^+$ phase. During the second peak at 100 K the FA molecules have reoriented to the pattern associated with the $a^-a^-c^+$ phase. This is the reason no phase transition is detected at 100 K when observing the mode activations since the activated modes are related to the Pb−I octahedra. Previous studies have also shown this result [34]. This shows that the NEP model was able to reproduce the results of FAPI as well [33].

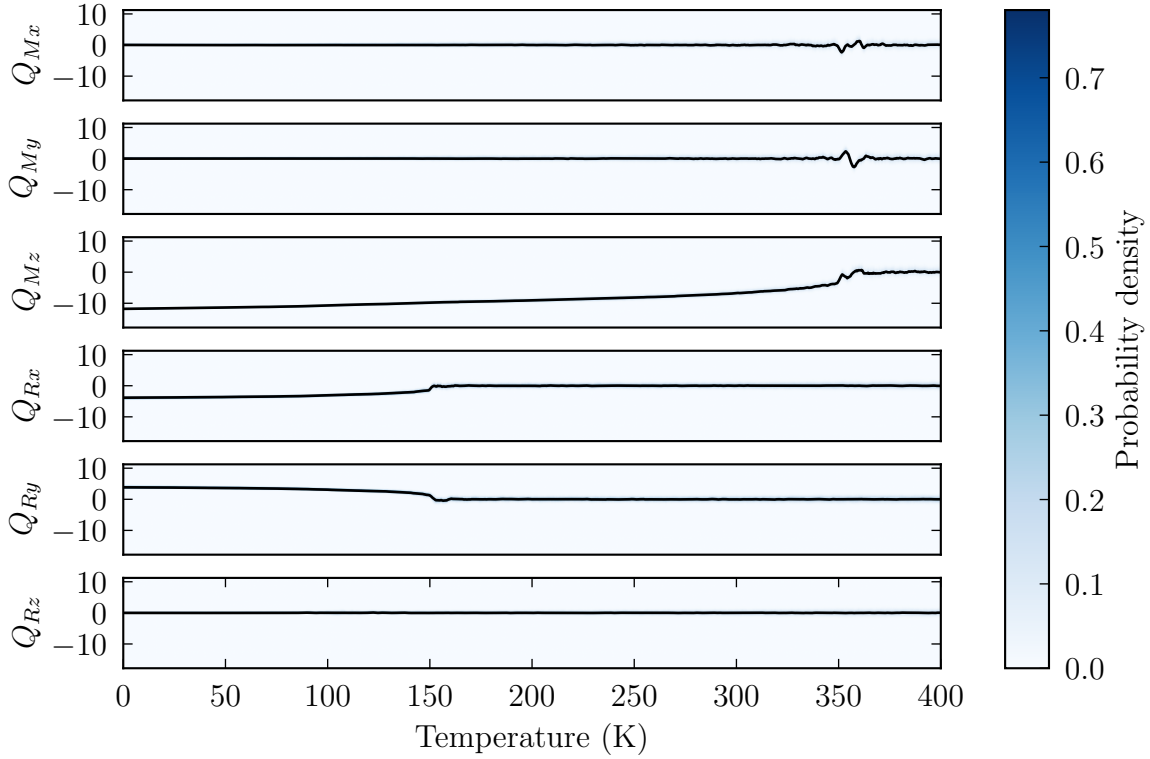

Figure 3.9: Mode projection of FAPI during cooling simulation starting from the the cubic phase ($a^0a^0a^0$). The average mode projection is represented as a black line.

3.2.3 Mixed MAPI-FAPI MD simulations

In the previous subsections it was shown that the NEP-model was able to predict both the behavior of MAPI and FAPI during a heating and cooling MD simulation. When mixing the two systems, the phase behavior is dependent on the proportions of the two materials. What is of special interest is the morphotropic phase boundary (MPB). It is created due to the tetragonal phases of MAPI and FAPI having different kinds of modes activated. As mentioned previously, MAPI favors a tetragonal phase with out-of-phase tilt ($a^0a^0c^-$), while FAPI favors a tetragonal phase with in-phase tilt ($a^0a^0c^+$). The MPB occurs at the proportion between MAPI and FAPI where the phases are energetically equally favorable. In this region the two phases can coexist in the crystal.
The MPB can be observed by calculating the proportion between M-mode (in-phase) and R-mode (out-of-phase) for different concentrations of FA. In Figure 3.10 this relation is plotted for multiple structures that were generated by randomly replacing FA molecules in a $16 \times 16 \times 16$ repetition of the FAPI unitcell with MA molecules and cooling the structures with a rate of 7 K/ns. The relation in Figure 3.10 is specifically for 250 K, however it appears to not change with temperature within the temperature frame in which both tetragonal phases coexists. The ratio between M- and R-modes in the lattice seems to follow a sigmoid relation with a rapid shift from one phase to another as the concentration of FA changes close to the MPB. A pattern of layers alternating between the two phases was observed. These layers

were located such that their norm was in the direction of activated modes. The MPB is found around 21% FA which is within the range of previous studies [9, 35, 36, 37]. The NEP-model can thus reproduce the phase behaviors of MAPI, FAPI and mixing of the materials.

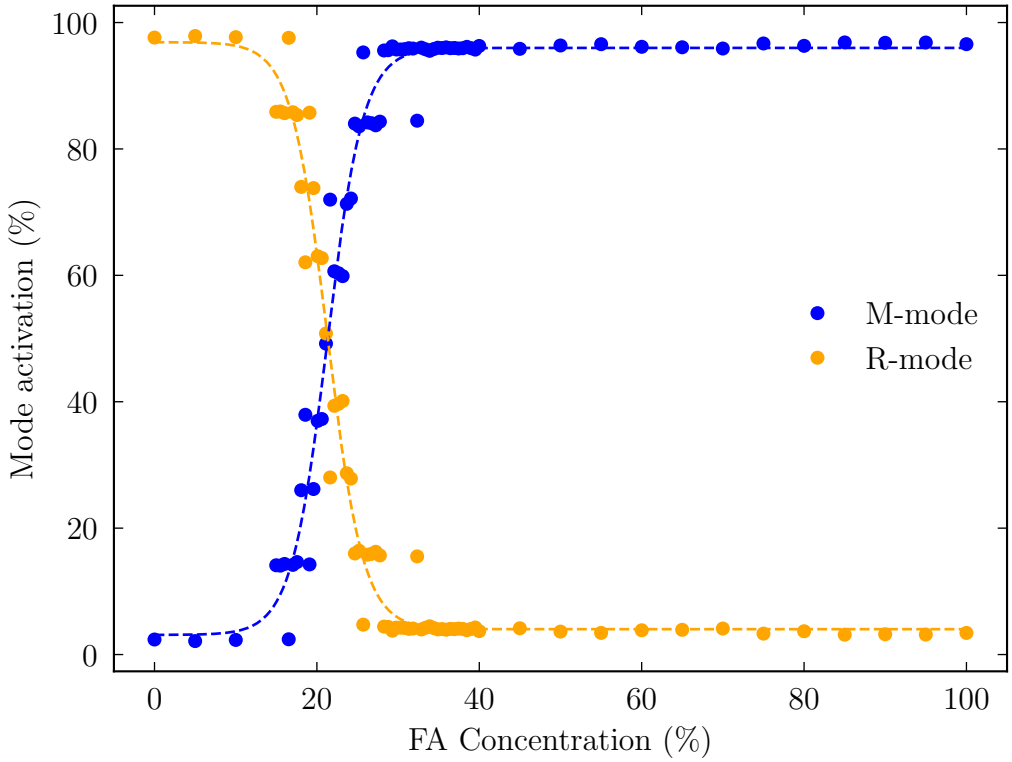

Figure 3.10: Percentage of total mode activation that is of M- and R-mode character for different concentrations of FA in $MA_xFA_{1-x}PI$.

3.3 GUAPI

To be able to analyse (MA,FA,GUA)PbI_3, the models performance for pure GUAPI also had to be analysed. Unlike MAPI and FAPI, this system is as previously mentioned less understood, since it generally does not form 3D perovskites. This makes it hard to study experimentally, but also makes it harder to achieve a stable NEP-model. However, with enough training structures and correct parameterising of the NEP-model it is possible to create a stable model. Since there is no experimental data to verify these results the purpose of studying how the model performs on pure GUAPI is to observe whether the model is stable and gives consistent results that are physically reasonable. Since it has already been verified with DFT that at least for smaller structures the model is accurate for pure GUAPI structures.

3.3.1 Finding the ground-state of GUAPI

To observe the phase behavior of pure GUAPI the ground-state first had to be found. This was done by first creating many different artificial distortions of the cubic GUAPI phase as well as randomly rotating the GUA molecules for $2 \times 2 \times 2$ repetitions of the unit cell. The resulting structures were then relaxed using BFGS to find the local minima of the PES that the NEP-model predicted. This random search was done one million times and the resulting structures were identified through mode projections. To further explore the PES to ensure that the global minimum had been found a local minima hopping search algorithm was implemented using the found local minima as starting structures. Minima hopping is a technique to explore a PES by heating the structure using short MD simulations. This can result in that the structure can jump over energy barriers and access new minima. Larger temperatures allows for more exploration. For that reason a feedback loop was implemented to decrease the temperature when the algorithm showed signs of exploration. In case the structural diversity of the search algorithm stagnated, the temperature was increased.

In Figure 3.11 it can be seen that the lowest energy structure found was $a^-a^-a^-$. It was also verified with DFT calculations that this was the lowest energy structure of the ones found. It can be seen that no tilt and out-of-phase tilt dominates. This is because most structure that have out-of-phase tilt has a much smaller magnitude compared to for instance the tetragonal phase of MAPI. This causes the structures to sometimes be classified as having no tilt, when in reality it just has a very weak tilt.

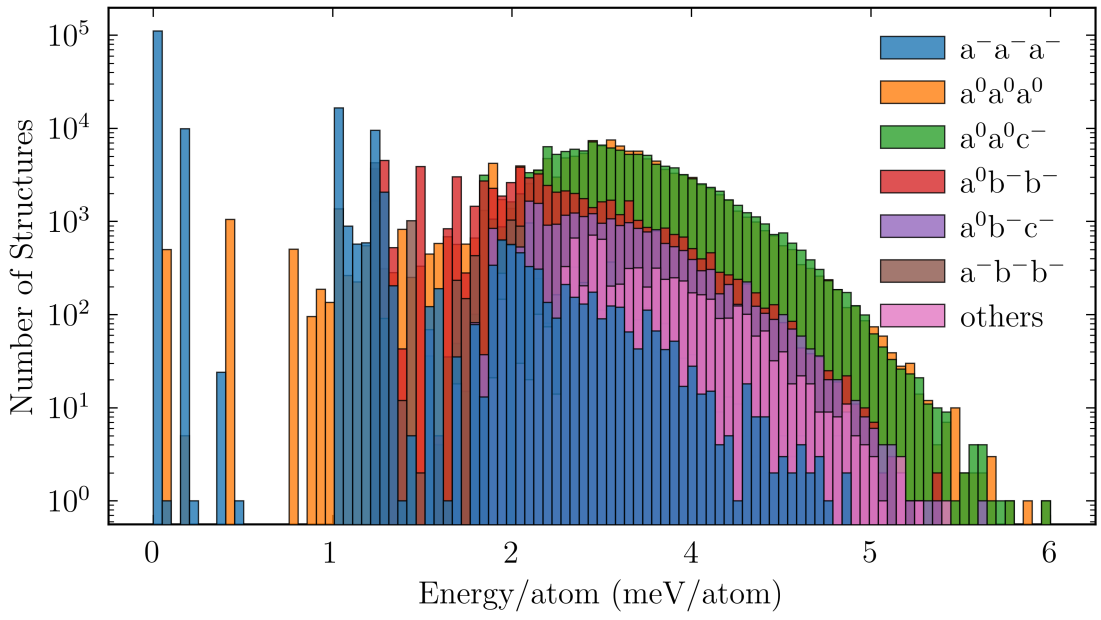

Figure 3.11: Energy distribution of the found minima and their Glazer notation.

3.3.2 GUAPI MD simulations

When the ground-state had been found, an MD analysis could be made in the same way as for MAPI and FAPI. Heating a $16 \times 16 \times 16$ repetition of the ground-state with a rate of 7 K/ns from 1 K to 400 K resulted in one phase transition around 310 K as can be seen in Figure 3.12. The high temperature phase could be classified as a cubic $a^0a^0a^0$ phase by observing the mode activations in Figure 3.13, which also seems to suggest that the transition is of first-order.

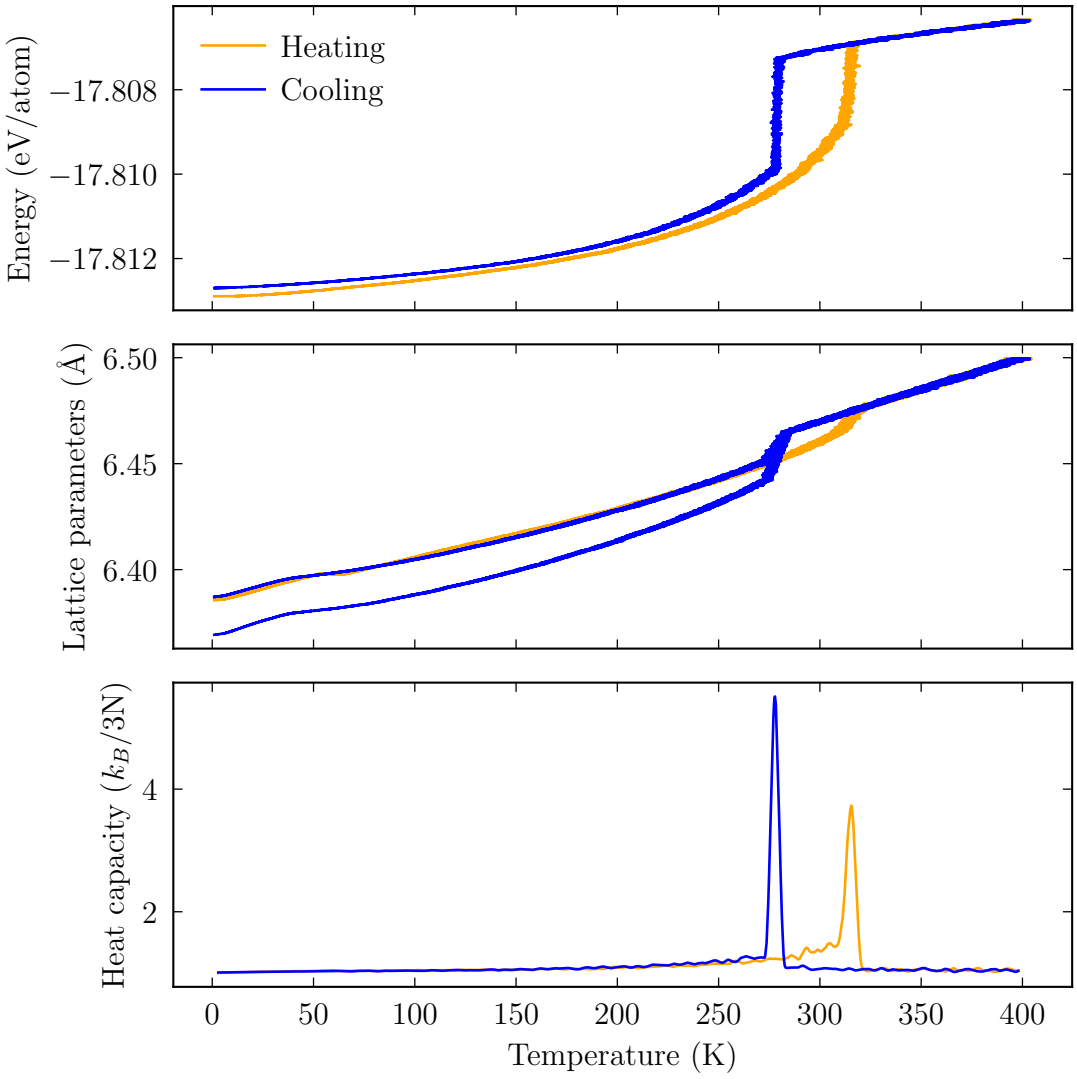

Figure 3.12: Potential energy, lattice parameters and heat capacity as a function of temperature of GUAPI.

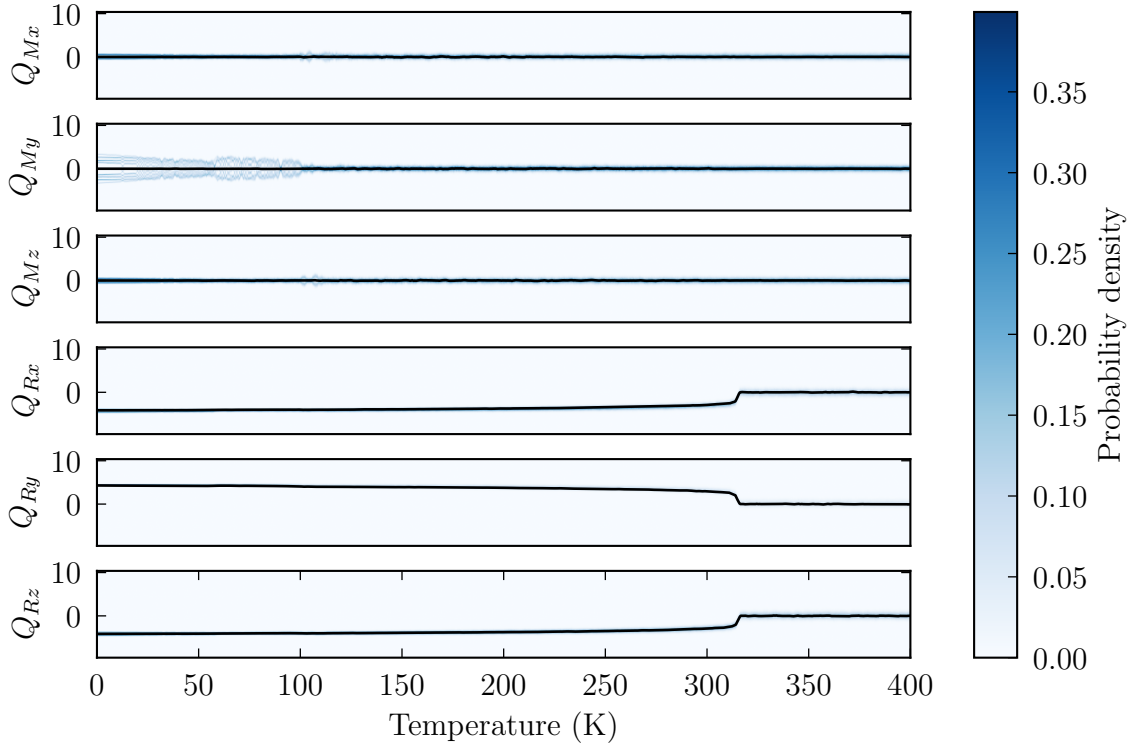

Figure 3.13: Mode projection of GUAPI during heating simulation starting from the ground-state ($a^-a^-a^-$). The average mode projection is represented as a black line.

The cubic phase achieved from the heating simulation was then cooled back to 1 K to observe the full transition cycle. In Figure 3.12 it seems like the ground-state is not recovered during cooling. However, upon investigation of the mode projections in Figure 3.14 the $a^-a^-a^-$ is actually recovered. The reason why it appears that the ground-state is not recovered is due to formation of phase boundaries in the $\langle 100 \rangle$ direction that have an M-mode behavior. These phase boundaries seem to be size related since they do not appear for smaller structures. For instance in the case of $12 \times 12 \times 12$ cells it appears that the ground-state is recovered since no phase boundaries are formed during the phase transition between the $a^0a^0a^0$ and $a^-a^-a^-$ phase which can be seen both through the observation of the potential energy in Figure 3.15 and the mode projections in Figure 3.16 and Figure 3.17. Another thing to note that occurs in both $16 \times 16 \times 16$ and $12 \times 12 \times 12$ cells is that the transition during the cooling process does not occur until 280 K, which is a notable shift from the heating simulation. Hysteresis is especially common in first-order transitions.

Even though phase boundaries did not form during the phase transition in for $12 \times 12 \times 12$ cell the ground-state had a tendency of having some activations of an M-mode for temperatures below 70 K both during heating and cooling. It seems to be a consequence of phase boundaries forming in the crystal. Unlike the previous phase boundaries, these phase boundaries are in the $\langle 011 \rangle$ direction. These boundaries also seem to be a consequence of the large size of the system, since they were not visible when searching for the ground-state.

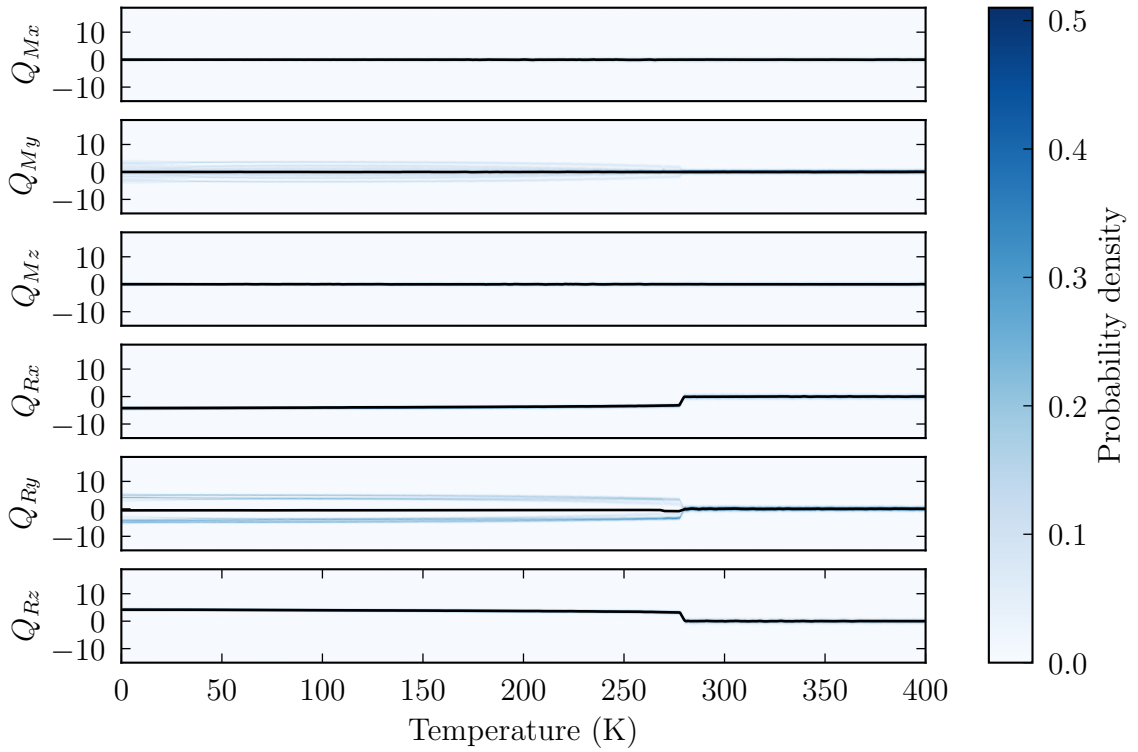

Figure 3.14: Mode projection of GUAPI during cooling simulation starting from the cubic phase ($a^0a^0a^0$). The average mode projection is represented as a black line.

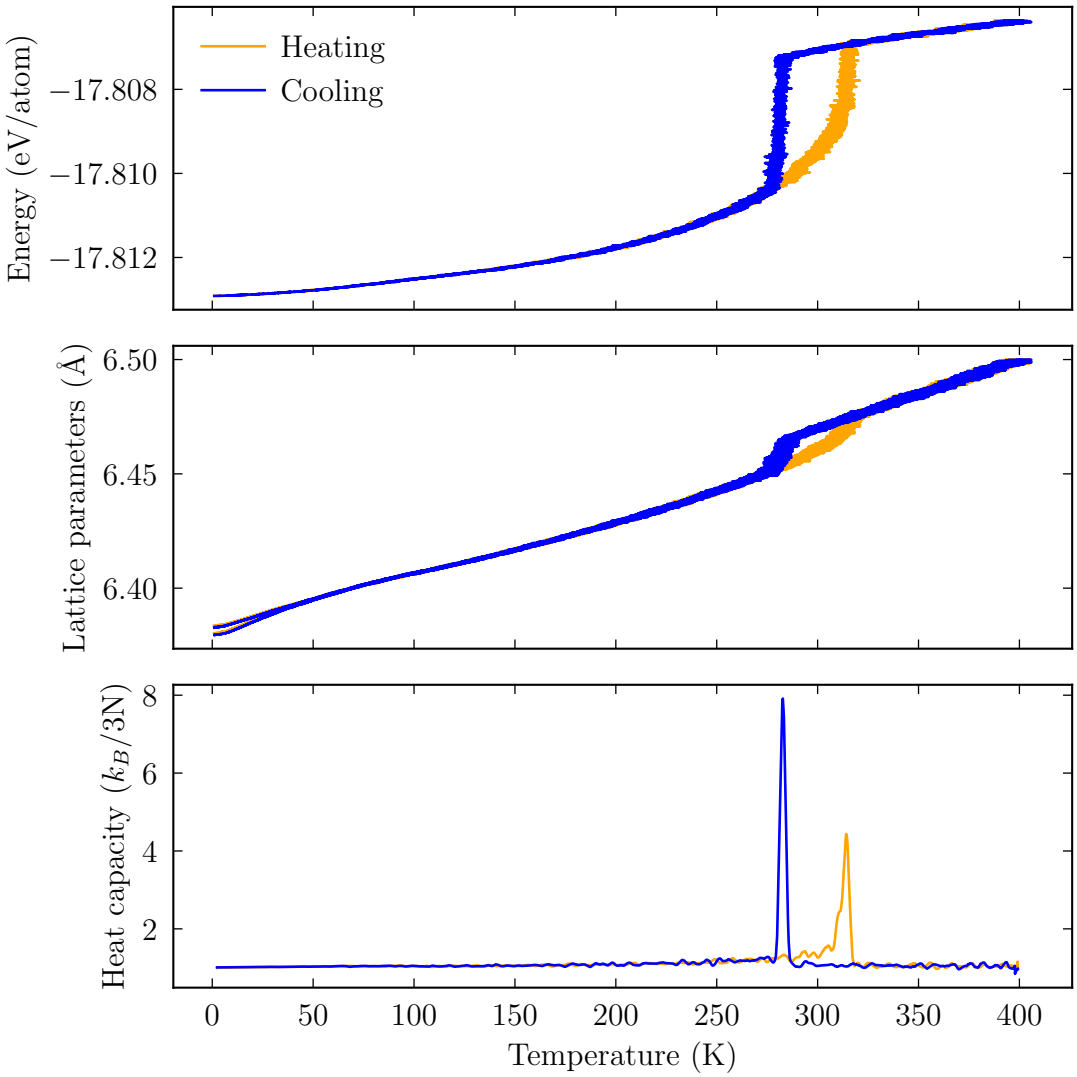

Figure 3.15: Potential energy, lattice parameters and heat capacity as a function of temperature of GUAPI. This is for a $12 \times 12 \times 12$ repetition of the unit cell.

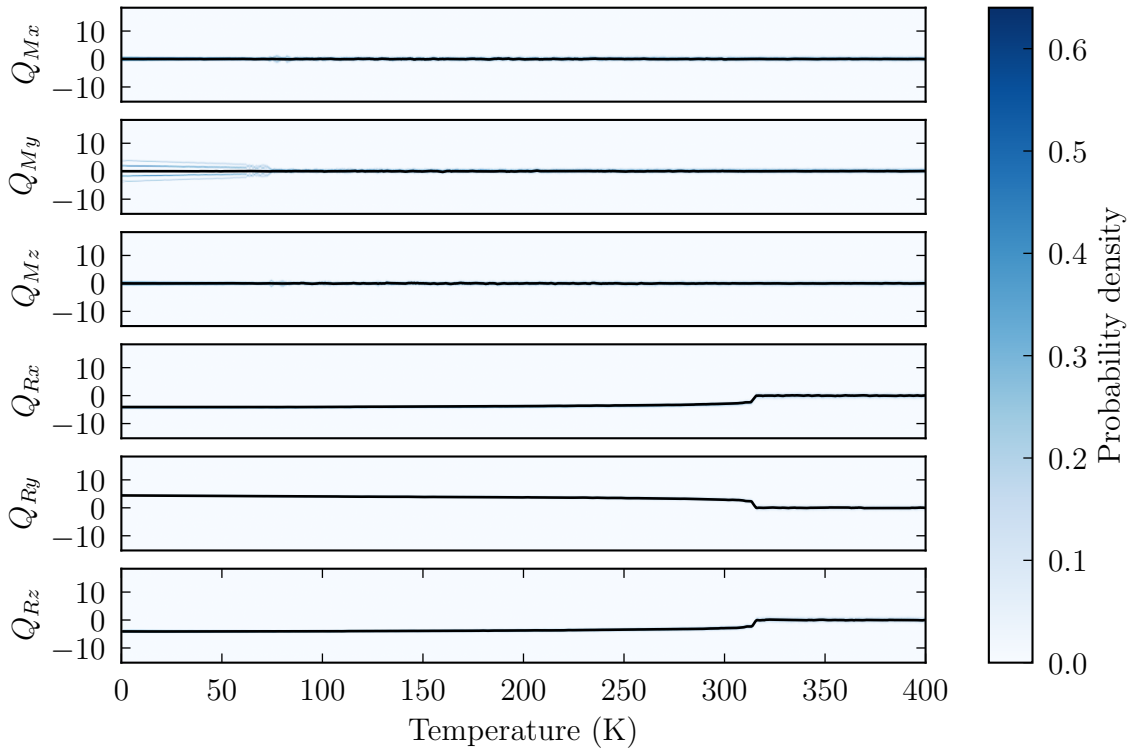

Figure 3.16: Mode projection of GUAPI during heating simulation starting from the ground-state ($a^-a^-a^-$). This is for a $12 \times 12 \times 12$ repetition of the unit cell. The average mode projection is represented as a black line.

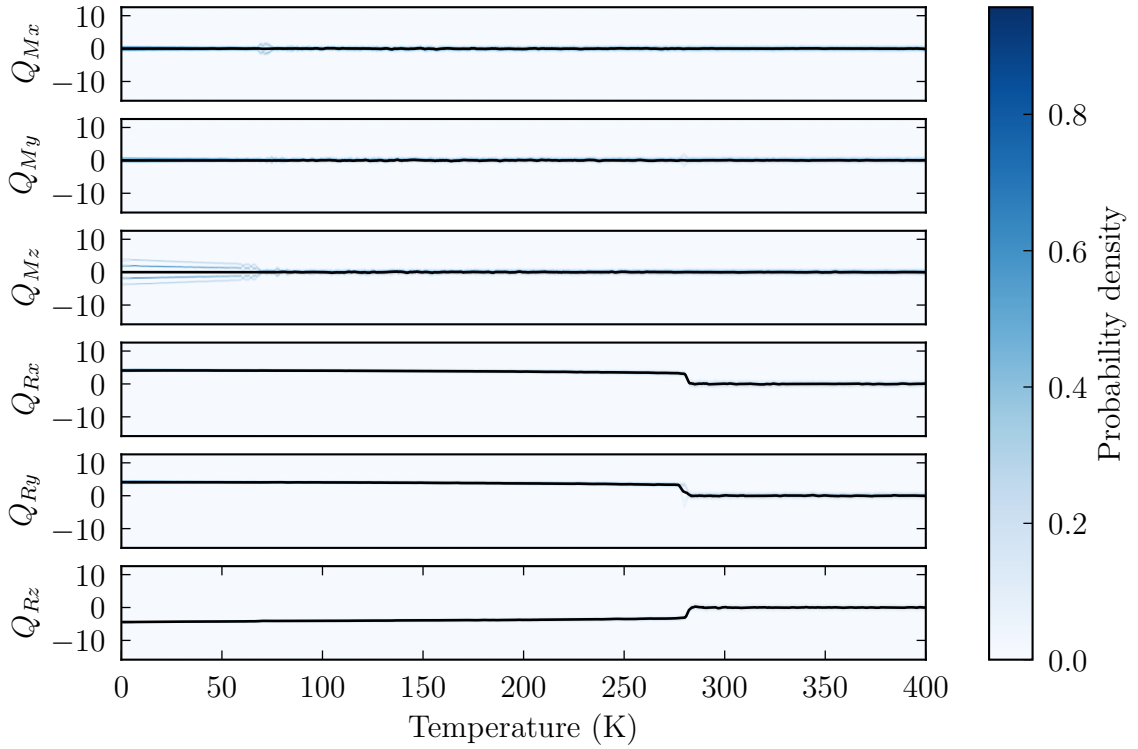

Figure 3.17: Mode projection of GUAPI during cooling simulation starting from the cubic phase ($a^0a^0a^0$). This is for a $12 \times 12 \times 12$ repetition of the unit cell. The average mode projection is represented as a black line.

3.3.2.1 Molecular orientation and rotational dynamics of GUA molecules

The previous analysis of the modes focuses on the lead-iodide lattice structure, but to understand the full phase dynamics of GUAPI the behavior of the GUA molecules has to be analysed as well. First of all the orientation of the GUA molecules can be analysed. The orientation of the molecule can be exactly defined through the calculation of two vectors. GUA has a geometry such that the three NH_2-groups are located in the same plane as can be seen in Figure 3.18. The norm of this plane was used as one of the defining vectors (it will be referred to as the A-vector) and one of the carbon-nitrogen vectors was used as the second defining vector.
The orientation of these two vectors was quantified using the spherical coordinates θ and ϕ. θ is defined as the polar angle and ϕ is the azimuthal angle. The orientation of all GUA molecules in the crystal at different temperatures during the cooling MD simulation was calculated and plotted as a heatmap in Figure 3.18. It can be seen that the cubic phase in the first row is correlated with mostly unordered GUA molecules. There is a pattern due to the constrains of the lattice on the molecules, but the pattern is significantly weaker than what can be seen for lower temperatures. This is reasonable since no symmetry breaking has occurred yet. As the perovskite transitions to the $a^-a^-a^-$ phase in the second row of Figure 3.18 a more confined pattern starts to emerge that is a subset of the higher probability regions in the cubic phase. The GUA molecule seems to lock into two different positions with equal probability. The two high probability orientations of the A-vector are simply the

same vector in opposite directions. This means that they define the same orientation of the GUA molecule. Looking at the carbon-nitrogen vector, six high probability orientations can be seen. These orientations are located along the same plane, which is reasonable since the A-vector is constrained to one direction. The reason why three orientations of the carbon-nitrogen bonds are prominent for each orientations of the GUA molecule is because there are three carbon-nitrogen bonds that can be picked with equal probability. Checking the specific values of orientations in the right column of Figure 3.18 it can be seen that the two dominant orientations of the GUA molecule are 60° rotations of the molecule around the A-vector. This is reasonable due to the alternating pattern of distorted iodide-lead lattice at lower temperatures. As the temperature decreases further, the pattern becomes even more prominent as more molecules lock into the highest probability regions. This is probably since these regions are more energetically favorable and thus when thermal fluctuations decreases the probability of molecules orienting in this particular pattern increases. Interestingly, the formation of the M-mode boundaries seems to be correlated with a further refinement of the GUA molecule into 6 specific orientations.

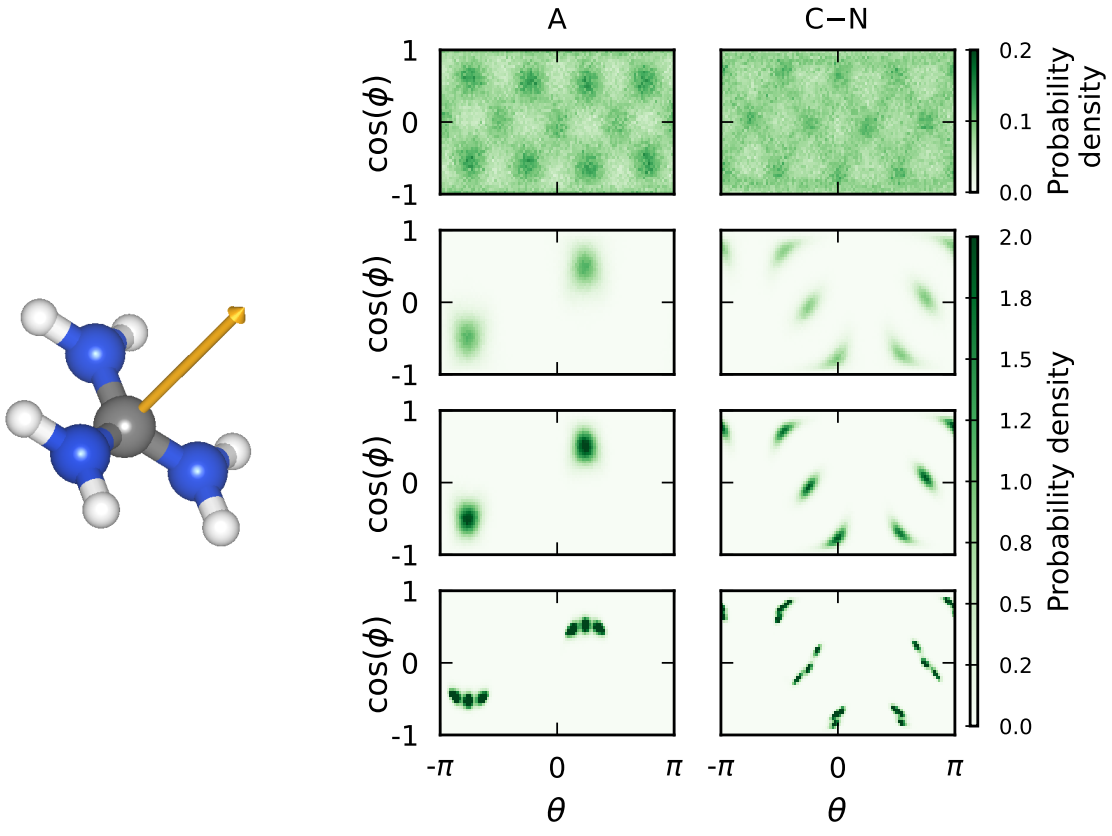

Figure 3.18: Orientation of the GUA molecules in GUAPI for 350 K, 200 K, 100 K and 20 K respectively from top to bottom. The left column shows the A-vector, which has been marked with orange in the illustration of the GUA molecule to the left. The right column shows one of the carbon-nitrogen bond vectors. Note that the A-vector is the norm of the plane spanned by the carbon-nitrogen bond vectors.

The rotational dynamics of the GUA molecules could be further investigated through the autocorrelation function of the A- and C-N-vectors. The autocorrelation function $C(\tau)$ is defined as

$$C(\tau) = \frac{\langle \mathbf{r}_B^i(t)\mathbf{r}_B^i(t+\tau)\rangle}{\langle \mathbf{r}_B^i(t)\mathbf{r}_B^i(t)\rangle}, \tag{3.2}$$

where $\mathbf{r}_B^i(t)$ is orientation vector B at time t for atom i.
MD simulations using the NVE ensemble were performed at constant temperature by first equilibrating structures from the cooling MD simulations using the NpT ensemble. Figure 3.19 shows that for increasing temperatures the autocorrelation time decreases. This is reasonable since heat induces stochastic motion. At lower temperatures the autocorrelation function is more or less constant, since the orientation of the GUA molecules becomes frozen in the low symmetry phase $a^-a^-a^-$ as previously seen in Figure 3.18. Furthermore the phase transition between $a^0a^0a^0$ and $a^-a^-a^-$ can be clearly seen by observing the rapid increase of the autocorrelation time around 280 K.

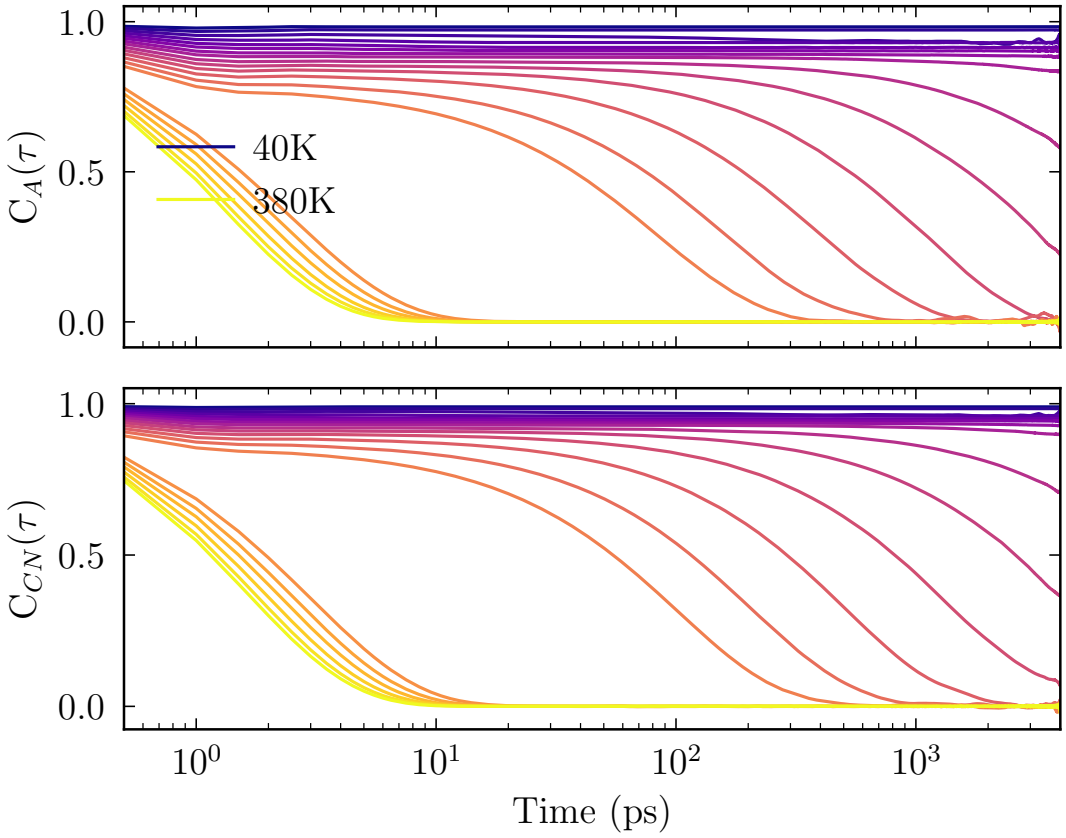

Figure 3.19: Autocorrelation function of the A-vector in the top image and C-N vector in the bottom image as a function of time.

The decay of the autocorrelation function can be modeled as $C(\tau) \propto e^{-\tau/\tau_{\text{rot}}}$, where τ_{rot} is the typical rotational time. This model is represented by the points in Figure 3.20. The data seems to follow one linear trend in the cubic phase and another in

the $a^-a^-a^-$ phase. This can be modeled with an Arrhenius behavior as $1/\tau_{\text{rot}}(T) \propto e^{-E_A/k_BT}$, where E_A is the activation energy of the rotation. The Arrhenius model is plotted as the dashed linear fit in Figure 3.20, which means that the tilt of the linear fit is the corresponding activation energy. In Figure 3.20 it can be seen that for both rotational degrees of freedom, the activation energy is notably larger in the $a^-a^-a^-$ phase than the cubic phase. This is reasonable since the symmetry breaking of the lattice constrains the GUA molecule.
This analysis of the GUA molecule shows that there is a strong correlation between the lattice and A-site dynamics of GUAPI with no notable delay, which is reasonable due to the large size of the GUA molecule, which should imply that it is strongly bonded to the lattice. Interestingly, when comparing with a similar study for FAPI, it was seen that the autocorrelation time was much smaller for FA at the same temperatures [33]. This is probably due to the large size and strong hydrogen-iodide bonds of the GUA molecule in GUAPI, which restricts rotational motion.

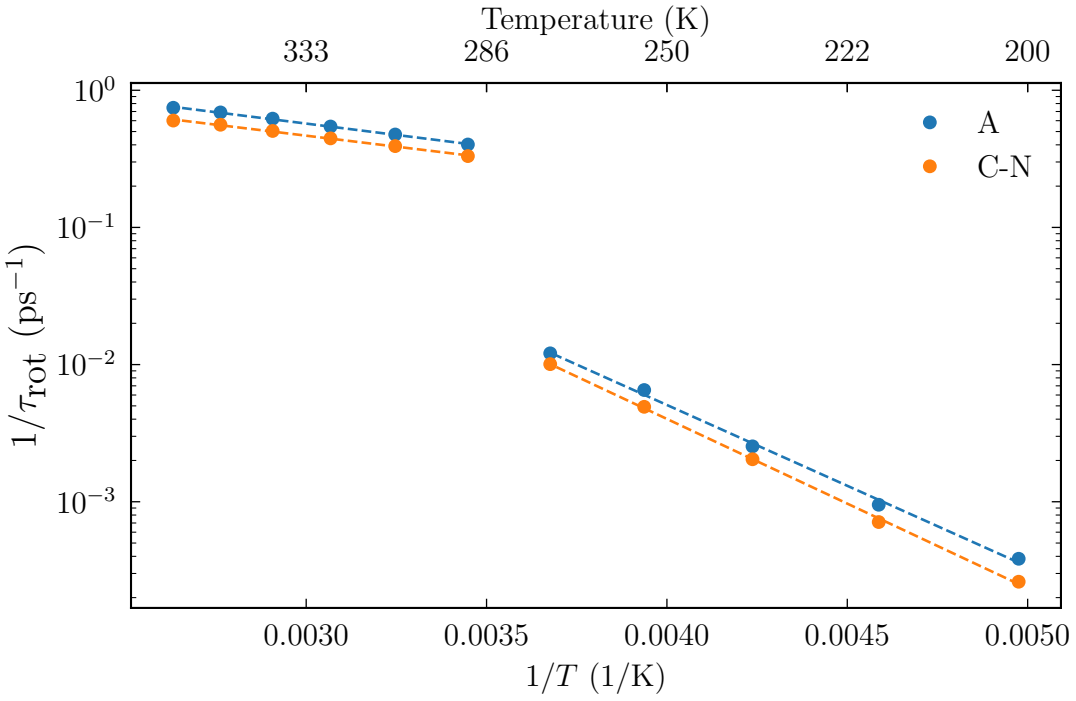

Figure 3.20: Rotational rate as a function of temperature for the A- and C-N-vector. For the cubic phase the activation barrier is 0.066 eV and 0.064 eV for the A- and C-N-vectors respectively, while for the $a^-a^-a^-$ phase the activation barrier is 0.234 eV and 0.245 eV for the A- and C-N-vectors respectively.

3.4 Triple cation simulations

The purpose of the NEP-model was ultimately to investigate the phase behavior of (MA,FA,GUA)PbI_3 systems. To achieve this, structures of a diverse range of proportions between the three cations were generated. These structures were then

cooled using MD from 400 K to 1 K. Unlike for pure materials the heating process was not investigated, since that would require to find the ground-state for each composition.
At 400 K every composition is cubic as can be seen in Figure 3.21, which is reasonable since the pure systems has already been identified to be in the cubic state at this temperature. Furthermore previous studies of mixed hybrid halide perovskites have not found any correlation between mixing and an increased temperature of the phase transition to cubic phase [9, 35].
Decreasing the temperature towards 300 K the tetragonal phase of pure MAPI and FAPI appears for low GUA concentrations. This is consistent with the pure simulations since pure MAPI and FAPI transition to the cubic phase above 300 K, while pure GUAPI has a phase transition to the cubic phase below 300 K. The MPB formed by the mixing of $a^0a^0c^+$ and $a^0a^0c^-$ shifts towards higher FA concentration as the amount of GUA increases. For instance at 0% GUA the MPB occurs at 21% FA as was also shown previously in Figure 3.10, while at 10% GUA the MPB occurs at 27% FA. This is reasonable since GUAPI favors out-of-phase tilt. Interestingly, this could mean that GUAPI drives the system more strongly towards out-of-phase tilt than MAPI. In the tetragonal phase, MAPI has a stronger R-mode than GUAPI, however GUAPI drives the system towards isotropic out of-phase tilt. The geometry of a 3D perovskite constrains an isotropic out-of-phase tilt to smaller amplitudes. This could imply that GUAPI preferably would drive the system towards larger out-of-phase tilt than MAPI, however is constrained by the geometry. This would explain why GUAPI shifts the MPB towards larger FA concentrations as well as the tendency of GUAPI to decay into lower dimensional perovskites in experiments. More mixing, especially in the case of low FA concentrations seems to drive the cubic phase transition towards lower temperatures. This has also been observed in studies of (MA,FA)-systems [9, 35].
This observation is further reinforced at 250 K where the $a^-a^-a^-$ phase appears for higher GUA concentration, but the cubic phase still exist for mixed systems. It primarily exists for systems of low MA concentrations. This could be caused by the competition between in-phase tilt and out-of-phase tilt preference of FAPI and GUAPI respectively, since a similar phenomenon occurs in mixed (MA,FA)-systems [9, 35].
The layered pattern caused by the mixing of MAPI and FAPI is present when adding GUAPI. However, there seems to be a correlation between an increasing amount of GUAPI and a weakening of the layered pattern. The weakening of the pattern could be caused by the pattern appearing in multiple directions. The appearance of the layered pattern in multiple directions is probably due to the preference of GUAPI for isotropic out-of-phase tilt.
The cubic phase completely disappears around 200 K. Mostly it is the $a^-a^-a^-$ phase region that expands between 250 K and 200 K. This is probably because the cubic region around 250 K was mostly influenced by GUA, since GUA had the lowest transition temperature to cubic phase. The phase boundaries mostly stay unchanged below 200 K with the mayor change being the transition of the $a^0a^0c^+$ phase to $a^-a^-c^+$.

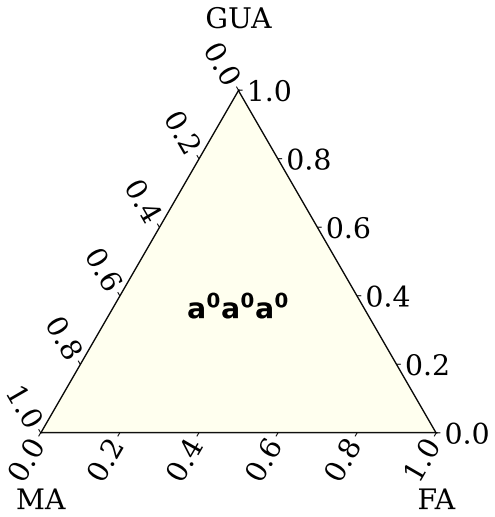

(a) Phases of (MA,FA,GUA)PbI_3 at 400 K.

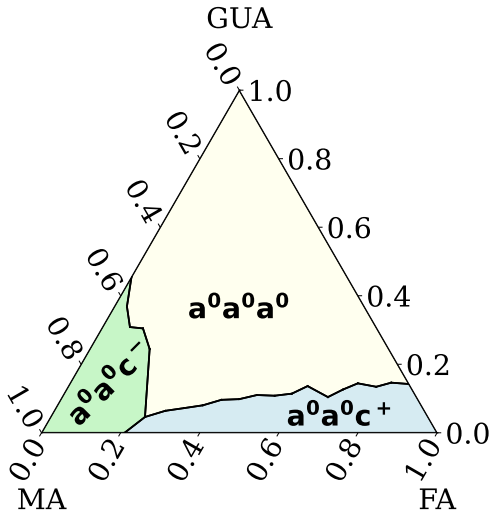

(b) Phases of (MA,FA,GUA)PbI_3 at 300 K.

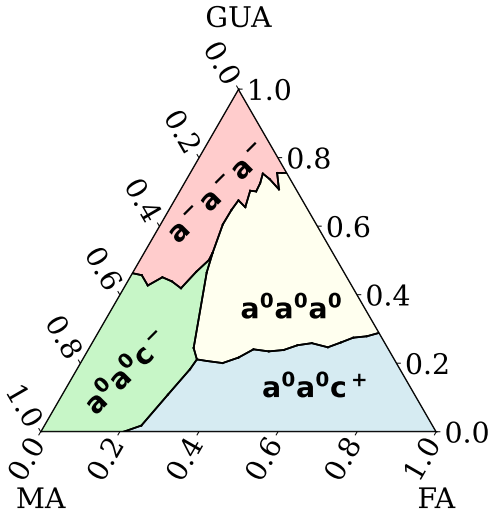

(c) Phases of (MA,FA,GUA)PbI_3 at 250 K.

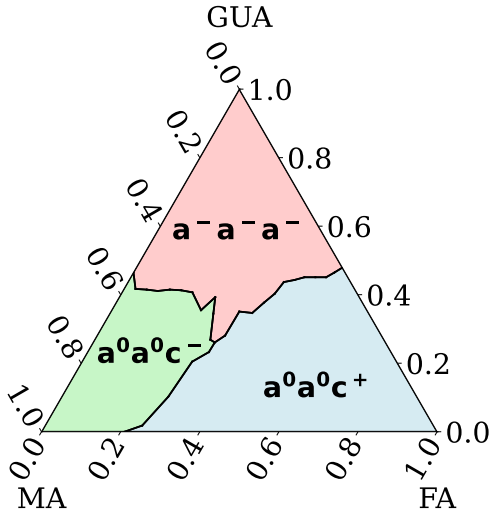

(d) Phases of (MA,FA,GUA)PbI_3 at 200 K.

Figure 3.21: Phase diagram of (MA,FA,GUA)PbI_3 at different temperatures.

4
Conclusion

This thesis shows that it is possible to train a NEP-model for hybrid halide perovskites containing GUA with an accuracy close to DFT.
The model could simulate a stable 3D perovskite phase of GUAPI. This could be done without compromising its performance for pure MAPI and FAPI, as well as mixed (MA,FA)PbI_3. For instance the model could recreate well known phase transitions for pure MAPI and FAPI as well as mixed (MA,FA)PbI_3. The layered pattern of $a^0a^0c^+$ and $a^0a^0c^-$ present in mixed (MA,FA)PbI_3 was also recreated.
The model predicts that the inclusion of GUA in mixed (MA,FA)PbI_3 systems tends to favor weak isotropic out-of-phase tilt, which can be denoted through Glazer notation as $a^-a^-a^-$. This results in a shift of the MPB between $a^0a^0c^+$ and $a^0a^0c^-$ towards higher FA concentrations. Furthermore the layered pattern is weakened, but starts appearing in multiple directions as GUA is added to the system.
Investigation of the orientation and rotational dynamics of the GUA molecule revealed that the molecule forms an alternating pattern of two orientations in the $a^-a^-a^-$ phase. The autocorrelation time in this phase is relatively low compared to for instance the FA molecule. This is probably due to the large size and many hydrogen atoms of the GUA molecule, which creates strong bonds to the lattice.
Future prospects could be to apply the model to larger systems of a few million atoms in order to investigate potential twinning patterns in the (MA,FA,GUA)PbI_3 systems.
The orientation and rotational dynamics of mixed systems could also be explored in case they differ from the pure materials. This could give further insight to the reason behind the phases forming in (MA,FA,GUA)PbI_3.
Furthermore, to apply the found results and possible future investigation of the phase behaviors to the design of perovskite solar cells it is also important to analyse the efficiency of these phases. This could for instance be done through calculations of the band structure to understand how the phases will interact with photons.

Bibliography

[1] A. K. Jena, A. Kulkarni, and T. Miyasaka. "Halide perovskite photovoltaics: Background, status, and future prospects". In: *Chemical Reviews* 119.5 (2019), pp. 3036–3103. DOI: 10.1021/acs.chemrev.8b00539.

[2] Guan-Woo Kim and Annamaria Petrozza. "Defect Tolerance and Intolerance in Metal-Halide Perovskites". In: *Advanced Energy Materials* 10.37 (2020), p. 2001959. DOI: https://doi.org/10.1002/aenm.202001959.

[3] Emmanuel A. Nyiekaa et al. "Development on inverted perovskite solar cells: A review". In: *Heliyon* 10.2 (2024), e24689. ISSN: 2405-8440. DOI: https://doi.org/10.1016/j.heliyon.2024.e24689.

[4] Sven Rühle. "Tabulated values of the Shockley–Queisser limit for single junction solar cells". In: *Solar Energy* 130 (2016), pp. 139–147. ISSN: 0038-092X. DOI: https://doi.org/10.1016/j.solener.2016.02.015.

[5] Aditya Mishra et al. "A Complete Picture of Cation Dynamics in Hybrid Perovskite Materials from Solid-State NMR Spectroscopy". In: *Journal of the American Chemical Society* 145.2 (2023), pp. 978–990. DOI: 10.1021/jacs.2c10149.

[6] Bethan Charles et al. "Understanding the stability of mixed A-cation lead iodide perovskites". In: *J. Mater. Chem. A* 5 (43 2017), pp. 22495–22499. DOI: 10.1039/C7TA08617B.

[7] Zheyong Fan et al. "GPUMD: A package for constructing accurate machine-learned potentials and performing highly efficient atomistic simulations". In: *The Journal of Chemical Physics* 157.11 (Sept. 2022), p. 114801. ISSN: 0021-9606. DOI: 10.1063/5.0106617.

[8] Ilyes Batatia et al. *A foundation model for atomistic materials chemistry*. 2025. URL: https://arxiv.org/abs/2401.00096.

[9] Tobias Hainer et al. *A Morphotropic Phase Boundary in $MA_{1-x}FA_xPbI_3$: Linking Structure, Dynamics, and Electronic Properties*. 2025. URL: https://arxiv.org/abs/2503.22372.

[10] Quinten A. Akkerman and Liberato Manna. "What Defines a Halide Perovskite?" In: *ACS Energy Letters* 5.2 (2020), pp. 604–610. DOI: 10.1021/acsenergylett.0c00039.

[11] Lili Gao, Ping Hu, and Shengzhong (Frank) Liu. "Low-dimensional perovskite modified 3D structures for higher-performance solar cells". In: *Journal of Energy Chemistry* 81 (2023), pp. 389–403. ISSN: 2095-4956. DOI: https://doi.org/10.1016/j.jechem.2023.01.061.

[12] P. Whitfield, N. Herron, and W. et al. Guise. “Structures, Phase Transitions and Tricritical Behavior of the Hybrid Perovskite Methyl Ammonium Lead Iodide”. In: *Sci Rep* 6 (2016), p. 35685. DOI: 10.1038/srep35685.

[13] A. M. Glazer. “The classification of tilted octahedra in perovskites”. In: *Acta Crystallographica Section B* 28.11 (1972), pp. 3384–3392. DOI: https://doi.org/10.1107/S0567740872007976.

[14] Zhen Li et al. “Stabilizing Perovskite Structures by Tuning Tolerance Factor: Formation of Formamidinium and Cesium Lead Iodide Solid-State Alloys”. In: *Chemistry of Materials* 28.1 (2016), pp. 284–292. DOI: 10.1021/acs.chemmater.5b04107.

[15] Jung-Hoon Lee et al. “Resolving the Physical Origin of Octahedral Tilting in Halide Perovskites”. In: *Chemistry of Materials* 28.12 (2016), pp. 4259–4266. DOI: 10.1021/acs.chemmater.6b00968.

[16] Pengfei Wu et al. “Magic guanidinium cations in perovskite solar cells: from bulk to interface”. In: *Mater. Chem. Front.* 7 (13 2023), pp. 2507–2527. DOI: 10.1039/D2QM01315K.

[17] Giacomo Giorgi et al. “Organic–Inorganic Hybrid Lead Iodide Perovskite Featuring Zero Dipole Moment Guanidinium Cations: A Theoretical Analysis”. In: *The Journal of Physical Chemistry C* 119.9 (2015), pp. 4694–4701. DOI: 10.1021/acs.jpcc.5b00051.

[18] Y.H. Kim et al. “Comprehensive defect suppression in perovskite nanocrystals for high-efficiency light-emitting diodes”. In: *Nature Photonics* 15 (2021), pp. 148–155. DOI: 10.1038/s41566-020-00732-4.

[19] Yi Ding et al. “Effects of guanidinium cations on structural, optoelectronic and photovoltaic properties of perovskites”. In: *Journal of Energy Chemistry* 58 (2021), pp. 48–54. ISSN: 2095-4956. DOI: https://doi.org/10.1016/j.jechem.2020.09.036.

[20] M. Ahart, M. Somayazulu, and R. et al. Cohen. “Origin of morphotropic phase boundaries in ferroelectrics”. In: *Nature* 451 (2008), pp. 545–548. DOI: 10.1038/nature06459.

[21] Hyun Woo Seo et al. “Revisiting the Shockley–Queisser Limit: Understanding Solar Cell Efficiency in One Sun and Indoor Environments”. In: *The Journal of Physical Chemistry Letters* 16 (2025), pp. 11795–11812. DOI: 10.1021/acs.jpclett.5c01792.

[22] S. Liu, V.P. Biju, and Y. et al. Qi. “Recent progress in the development of high-efficiency inverted perovskite solar cells”. In: *NPG Asia Mater* 15 (2023), p. 27. DOI: 10.1038/s41427-023-00474-z.

[23] Feliciano Guistino. *Materials Modelling using Density Functional Theory*. 1st. Oxford, United Kingdom: Oxford University Press, 2014. ISBN: 978-0-19-966243-2.

[24] W. Koch and M.C. Holthausen. “The Hohenberg-Kohn Theorems”. In: *A Chemist’s Guide to Density Functional Theory*. John Wiley Sons, Ltd, 2001. Chap. 4, pp. 33–40. ISBN: 9783527600045. DOI: https://doi.org/10.1002/3527600043.ch4.

[25] F. Zahariev, S. S. Leang, and Mark S. Gordon. “Functional derivatives of meta-generalized gradient approximation (meta-GGA) type exchange-correlation

density functionals". In: *The Journal of Chemical Physics* 138.24 (June 2013), p. 244108. ISSN: 0021-9606. DOI: 10.1063/1.4811270.

[26] Daan Frenkel and Berend Smit. *Understanding Molecular Simulation*. 2nd. San Diego, California: Academic Press, 2002. ISBN: 978-0-12-267351-1. DOI: 10.1016/B978-0-12-267351-1.X5000-7.

[27] Zheyong Fan et al. "Neuroevolution machine learning potentials: Combining high accuracy and low cost in atomistic simulations and application to heat transport". In: *Phys. Rev. B* 104 (10 Sept. 2021), p. 104309. DOI: 10.1103/PhysRevB.104.104309.

[28] Tom Schaul, Tobias Glasmachers, and Jürgen Schmidhuber. "High dimensions and heavy tails for natural evolution strategies". In: *Proceedings of the 13th Annual Conference on Genetic and Evolutionary Computation*. GECCO '11. Dublin, Ireland: Association for Computing Machinery, 2011, pp. 845–852. ISBN: 9781450305570. DOI: 10.1145/2001576.2001692.

[29] Ilyes Batatia et al. *MACE: Higher Order Equivariant Message Passing Neural Networks for Fast and Accurate Force Fields*. 2023. DOI: 10.48550/arXiv.2206.07697.

[30] Stuart Thomson. *Observing Phase Transitions in a Halide Perovskite Using Temperature Dependent Photoluminescence Spectroscopy*. May 2018.

[31] A. Mattoni et al. "Methylammonium Rotational Dynamics in Lead Halide Perovskite by Classical Molecular Dynamics: The Role of Temperature". In: *The Journal of Physical Chemistry C* 119.30 (2015), pp. 17421–17428. DOI: 10.1021/acs.jpcc.5b04283.

[32] Erik Fransson et al. "Revealing the Free Energy Landscape of Halide Perovskites: Metastability and Transition Characters in CsPbBr3 and MAPbI3". In: *Chemistry of Materials* 35.19 (2023), pp. 8229–8238. DOI: 10.1021/acs.chemmater.3c01740.

[33] Sangita Dutta et al. "Revealing the Low-Temperature Phase of FAPbI3 Using a Machine-Learned Potential". In: *Journal of the American Chemical Society* 0.0 (0), null. DOI: 10.1021/jacs.5c05265.

[34] Shiro Kawachi et al. "Structural and Thermal Properties in Formamidinium and Cs-Mixed Lead Halides". In: *The Journal of Physical Chemistry Letters* 10.22 (2019), pp. 6967–6972. DOI: 10.1021/acs.jpclett.9b02750.

[35] Adrián Francisco-López et al. "Phase Diagram of Methylammonium/Formamidinium Lead Iodide Perovskite Solid Solutions from Temperature-Dependent Photoluminescence and Raman Spectroscopies". In: *The Journal of Physical Chemistry C* 124.6 (2020), pp. 3448–3458. DOI: 10.1021/acs.jpcc.9b10185.

[36] Hongge Zheng et al. "Temperature-dependent photoluminescence properties of mixed-cation methylammonium–formamidium lead iodide [HC(NH2)2]x[CH3NH3]1xPbI3 perovskite nanostructures". In: *J. Mater. Chem. C* 5 (46 2017), pp. 12057–12061. DOI: 10.1039/C7TC04146B. URL: http://dx.doi.org/10.1039/C7TC04146B.

[37] Ashutosh Mohanty et al. "Phase Diagram and Dielectric Properties of MA1–xFAxPbI3". In: *ACS Energy Letters* 4.9 (2019), pp. 2045–2051. DOI: 10.1021/acsenergylett.9b01291.

DEPARTMENT OF CONDENSED MATTER PHYSICS
CHALMERS UNIVERSITY OF TECHNOLOGY
Gothenburg, Sweden
www.chalmers.se

CHALMERS
UNIVERSITY OF TECHNOLOGY